

The Cosmic Baryon and Metal Cycles

Céline Péroux^{1,2} and J. Christopher Howk³

¹European Southern Observatory, Karl-Schwarzschild-Str. 2, 85748

Garching-bei-München, Germany; email: cperoux@eso.org

²Aix Marseille Université, CNRS, LAM (Laboratoire d'Astrophysique de Marseille) UMR 7326, 13388, Marseille, France

³Department of Physics, University of Notre Dame, Notre Dame, IN 46556, USA; email: jhowk@nd.edu

Annual Review of Astronomy and
Astrophysics 2020. AA:1–47

[https://doi.org/10.1146/\(\(please add article doi\)\)](https://doi.org/10.1146/((please add article doi)))

Copyright © 2020 by Annual Reviews.
All rights reserved

Keywords

baryon density, atomic and molecular gas, cosmic abundances, galaxy chemical evolution, interstellar dust, quasar absorption line spectroscopy

Abstract

Characterizing the relationship between stars, gas, and metals in galaxies is a critical component of understanding the cosmic baryon cycle. We compile contemporary censuses of the baryons in collapsed structures, their chemical make-up and dust content. We show that:

- The H I mass density of the Universe is well determined to redshifts $z \approx 5$ and shows minor evolution with time. New observations of molecular hydrogen reveal its evolution mirrors that of the global star formation rate density. The constant cosmic molecular gas depletion timescale points to a universal relationship between gas reservoirs and star formation.
- The metal mass density in cold gas ($T \lesssim 10^4$ K) contains virtually all the metals produced by stars for $z \gtrsim 2.5$. At lower redshifts, the contributors to the total amount of metals are more diverse; at $z < 1$, most of the observed metals are bound in stars. Overall there is little evidence for a “missing metals problem” in modern censuses.
- We characterize the dust content of neutral gas over cosmic time, finding the dust-to-gas and dust-to-metals ratios fall with decreasing metallicity. We calculate the cosmological dust mass density in the neutral gas up to $z \approx 5$. There is good agreement between multiple tracers of the dust content of the Universe.

Contents

| | |
|---|----|
| 1. CONTEXT | 2 |
| 1.1. Motivation of this Review | 2 |
| 1.2. Probing Baryons and Metals | 3 |
| 1.3. Basic Concepts of Absorption | 6 |
| 2. COSMIC EVOLUTION OF BARYONS | 8 |
| 2.1. Cosmic Evolution of Neutral Gas | 8 |
| 2.2. Cosmic Evolution of Molecular Gas | 13 |
| 2.3. Cosmic Evolution of Condensed Matter | 14 |
| 3. COSMIC EVOLUTION OF METALS | 20 |
| 3.1. Basic Principles of Measuring Metallicity through Absorption Lines | 20 |
| 3.2. Challenges in Assessing Metallicity | 20 |
| 3.3. Building Statistical Samples of Cosmic Metals | 23 |
| 3.4. Cosmic Evolution of Neutral Gas Metallicity | 23 |
| 3.5. Census of Metals in the Universe | 24 |
| 4. COSMIC EVOLUTION OF DUST | 31 |
| 4.1. Basic Principles of Assessing the Dust in the Universe | 32 |
| 4.2. Cosmological Dust Mass Densities | 33 |
| 5. LOOKING FORWARD AND CONCLUSIONS | 37 |
| 5.1. Pushing from the global to the local | 37 |
| 5.2. Simulating Baryonic Processes in Cosmological Context | 39 |
| 5.3. Concluding Remarks | 40 |

1. CONTEXT

1.1. Motivation of this Review

Astronomers now know the basic constituents of the present Universe: 73% dark energy, 23% dark matter, 4% in baryons. The term *baryons* is used to refer to the normal matter of the Universe (inclusive of the baryonic and leptonic matter discussed by physicists). The baryon density parameter – the comoving baryon density normalized to the critical density, $\Omega_{\text{baryons}} \equiv \rho_{\text{baryons}}/\rho_{\text{crit},0}$ – that describes the quantity of normal matter is a fundamental cosmological parameter. One of the great successes of the last decades is the excellent agreement between estimates of Ω_{baryons} from primordial nucleosynthesis (Cooke et al. 2018) and Cosmic Microwave Background anisotropies (Planck Collaboration et al. 2016). From the Big Bang onwards, the baryons collapse with dark matter to form the large-scale structure, galaxies, and stars we observe. While their mass grows with time, only a minority of the baryonic matter is found in stars – even today, some 13.7 Gyr after the Big Bang, > 90% of the baryons are found in the gaseous phase of the Universe. The gas, notably the cold gas traced by H I and H₂, provides the reservoir of fuel for forming stars.

The formation of stars leads naturally to the creation of *metals* – the elements heavier than helium. The study of the metal content in cosmic environments provides fundamental insights into the evolutionary processes that drive the formation and evolution of galaxies and the stars within them. Metals are largely created in stellar interiors through nuclear fusion reactions. They are expelled from stars through the supernova explosions that mark the ends of massive stars’ lives. The collective effects of supernovae also serve to distribute

Baryons: Normal matter

Metals: Elements heavier than helium

Metallicity: Relative quantity of metal atoms compared to hydrogen

Dust: Solid-phase materials composed of metals

the metals on much larger scales: mixing metals into the interstellar medium (ISM) of galaxies and even beyond. The metals that remain in the ISM are incorporated into the next generation of stars. This includes the metals chemically sequestered into dust grains, the solid phase material that plays a central role in catalyzing formation of the molecules essential to star formation.

Observations of the temporal and spatial evolution of metals are key to constraining this global picture of the Universe’s evolution. Early accounting of the total metal budget found an order of magnitude shortfall in the comoving density of observed metals compared with those expected to be produced by the stellar content of the Universe (Pettini 1999; Pagel 1999). This so-called “*missing metals problem*” was originally based on metal abundances derived for components of the Universe at $z = 2.5$, including gas traced by quasar absorbers and galaxies. It was then postulated that the missing metals would be found far from their production sites, in the hot gas filling galactic halos and proto-clusters. This problem has been revisited several times (e.g., Ferrara et al. 2005; Bouché et al. 2005, 2006, 2007; Shull et al. 2014).

This review synthesizes modern censuses of gas, metals, and dust in the baryonic components most closely related to galaxies and their star formation. By gathering the latest robust observations and state-of-the-art, physically motivated cosmological hydrodynamical models of galaxy formation, we assess these quantities continuously with look-back time over 90% of the age of the Universe. Given the limited space available, it is impossible to provide a thorough survey of such a huge community effort without leaving out significant contributions or whole subfields. Specifically in this volume, Tacconi et al. (2020) offers an alternative view of the molecular and dust content of galaxies, and Forster-Schreiber (2020) focuses on the kinematics and resolved metal content of intermediate redshift galaxies. In what follows we focus on a series of questions: How does the gas reservoir which fuels star formation evolve (§2)? Where are the metals in the Universe (§3)? What is the cosmic evolution of dust mass (§4)? In the final section, §5, we provide a forward looking view of the field.

All results presented here assume a concordance Λ CDM cosmology with parameters $(\Omega_M, \Omega_\Lambda, h) = (0.3, 0.7, 0.7)$, where Ω_M and Ω_Λ are the normalized mass-energy densities of matter and the cosmological constant, respectively, at $z = 0$ relative to the critical density, $\rho_{\text{crit},0} \equiv 8\pi G/3H_0^2$. The quantity $h \equiv H_0/(100 \text{ km s}^{-1} \text{ Mpc}^{-1})$ is a dimensionless statement of the present-day Hubble constant, H_0 . We use comoving coordinates when discussing volume densities throughout this work, such that a comoving Mpc, cMpc, is related to the physical (proper) distance by $\text{cMpc} \equiv \text{Mpc} \times (1+z)$. All logarithms assume base-10.

1.2. Probing Baryons and Metals

Only a minority of the baryons are scrutinized by observations of starlight from galaxies. The remaining baryons reside in low-density gas which is challenging to detect in emission (Wijers et al. 2019; Augustin et al. 2019). The baryons and metals associated with the majority of the gas that lies beyond the regions excited by hot stars is studied using resonant absorption lines in the spectra of background sources. This is a particularly powerful technique when using bright background sources such as quasars, gamma ray bursts (GRBs) (Bolmer et al. 2019), fast radio burst (FRBs) (Prochaska & Zheng 2019), or even other galaxies (Cooke & O’Meara 2015; Péroux et al. 2018). Absorption lines provide a measure

ISM: Interstellar Medium

CGM: Circumgalactic Medium

IGM: Intergalactic Medium

WHIM: Warm-Hot Intergalactic Medium

Mass densities: ρ_X is the *comoving* mass density for a component X (in $\text{M}_\odot \text{ cMpc}^{-3}$).

Density parameters: Ω_X is the density normalized by the critical density at $z = 0$, $\Omega_X \equiv \rho_X/\rho_{\text{crit},0}$ (unitless).

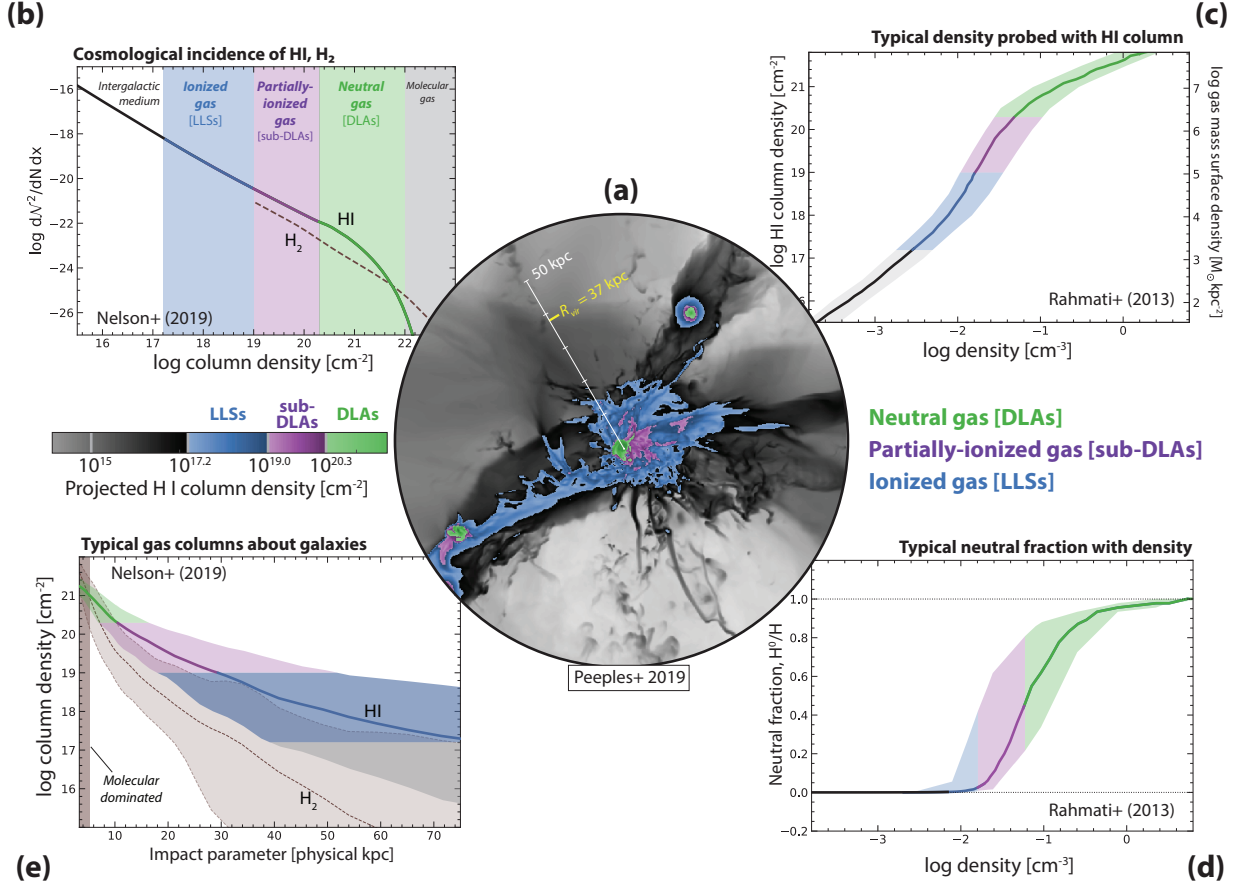


Figure 1

A broad view of the physical properties of cold gas discussed in this review and its relationship to galaxies. This figure summarizes the behavior of gas column (surface) densities in $z \sim 2 - 3$ simulated galaxy halos. The central panel (a) shows projected gas column densities for a halo that will develop into a Milky Way-mass system by $z = 0$. The H I column densities are coded according to the scale in the middle-left, and the color-coding for all panels is summarized in the middle-right. The four sub-panels show (b) the cosmological column density distribution, (c) the typical projected H I column density as a function of total particle density, (d) the neutral fraction of the gas as a function of particle density, and (e) the typical column density of H I and H₂ as a function of projected distance from simulated galaxies. The rarer high column density (and thus highest density / least ionized) gas is preferentially found in the inner regions of galaxies.

of the surface density or *column density* of atoms (molecules) between the observer and the background source (expressed in atoms cm⁻²). The H I column density, for example, along a sightline passing through gas with a neutral hydrogen particle density, n_{HI} (in atoms cm⁻³) is

$$N(\text{H I}) \equiv \int n_{\text{HI}} ds, \quad 1.$$

where s is the path the sightline takes through the gas. The important advantage of absorption over emission from galaxies is the ability to reach low gas densities. Moreover, the sensitivity of this technique is redshift independent and offers a powerful tool to study the cosmic evolution of the baryon and metal content of the Universe. While individual absorption measurements are limited to a pencil-beam along the line-of-sight, the large samples now assembled allow us to statistically measure the mean properties of galaxies by combining many lines of sight, thereby also minimizing cosmic variance effects.

In Figure 1 we highlight the physical properties of the gas that is studied in absorption, focusing on the high column density gas in and around galaxies. We focus this review on these densest environments, which play a key role in the baryon cycle of galaxies and harbor the majority of the metals in the Universe. The central panel, Figure 1a, shows the projected H I column density, $N(\text{H I})$, around a typical simulated galaxy at $z = 2$ (from the Enzo-based FOGGIE suite of Peebles et al. 2019). The remaining panels in Figure 1 connect the gas’ physical properties (notably its density and ionization conditions) with its environment and measurable properties (in this case drawn from the analysis of the EAGLE and IllustrisTNG simulations in Rahmati et al. 2013 and Nelson et al. 2019, respectively). Clear trends emerge when examining in Figure 1. The higher column densities are found closer to the centers of simulated galaxies (Figure 1e), and high column density gas is denser (Figure 1c) and more neutral (Figure 1d). Because higher column density gas has a smaller sky cross section, the frequency with which random sight lines in “blind” surveys intercept this gas is smaller than for lower column densities (Figure 1b).

The highest H I column densities in Figure 1 trace dense gas and are largely self-shielded from ionizing ultraviolet background photons, thus remaining mostly neutral. We identify *neutral gas* regions in this review as those having H I column densities $N(\text{H I}) > 2 \times 10^{20} \text{ cm}^{-2}$, often referred to as Damped Lyman- α Systems or DLAs (see review by Wolfe et al. 2005). These systems trace both the cold and warm neutral medium.¹ This canonical definition was introduced by Wolfe et al. (1986) because such column densities are characteristic of H I 21-cm measurements of local disk galaxies while providing lines of sufficient equivalent width (§1.3) to be easily detectable in the low-resolution spectra available at the time.

Lower H I surface density gas found further from the cores of galaxies (Figure 1e) is increasingly more ionized and multi-phase (Figure 1e). The ionization state of hydrogen is set by the balance of the reaction



The optical depth at the Lyman limit ($h\nu = 1 \text{ Ryd} \approx 13.6 \text{ eV}$ or $\lambda \approx 912 \text{ \AA}$) is key: high optical depths at energies $\sim 1 - 2 \text{ Ryd}$ keep ionizing photons (γ) from propagating throughout the gas. For $10^{19} \leq N(\text{H I}) \leq 2 \times 10^{20} \text{ cm}^{-2}$, the gas contains a mixture of neutral and ionized H, and we refer to such regions as *partially-ionized gas* throughout this review. This column density regime corresponds to the *sub-DLAs* first denoted by Péroux et al. (2003), who set the column density definition to include all systems which contribute significantly to the total H I mass density. These systems are sometimes referred to as *super Lyman-limit systems*.

¹Here we are using the nomenclature “neutral gas” to refer specifically to the atomic component; we consider the molecular component of the coldest gas separately.

molecular gas:

$$N(\text{H}_2) \geq N(\text{H I})$$

neutral gas (DLAs):

$$N(\text{H I}) \geq 10^{20.3} \text{ cm}^{-2}$$

partially-ionized gas (sub-DLAs):

$$N(\text{H I}) = 10^{19.0} - 10^{20.3} \text{ cm}^{-2}$$

ionized gas (LLS):

$$N(\text{H I}) = 10^{17.2} - 10^{19.0} \text{ cm}^{-2}$$

At lower column densities, we designate systems with $1.6 \times 10^{17} \leq N(\text{H I}) < 10^{19} \text{ cm}^2$ as *ionized gas*. These are the Lyman-limit systems (LLSs; Tytler 1982), where the lower bound corresponds to an optical depth at the Lyman limit $\tau_{912} \geq 1$. Observations and modeling of metal lines from these absorbers demonstrate they trace ionized structures, with a neutral fraction often $\text{H}^0/\text{H} \approx 10^{-3}$ (Figure 1e; cf. Fumagalli et al. 2016; Wotta et al. 2019). These absorbers are easily identifiable by their distinctive absorption break in quasar spectra (see Figure 2). These lower-density absorbers are found in more extended regions around galaxies (Figure 1a, d) and are subsequently observed with a higher frequency than the higher column density systems (Figure 1b).

At even lower column (surface) densities, the gas becomes optically thin to ionizing radiation and traces low-density circumgalactic and intergalactic gas. The IGM manifests itself observationally as a “forest” of H I absorption lines in the spectra of background quasars, with $10^{12} \leq N(\text{H I}) \leq 1.6 \times 10^{17} \text{ cm}^2$, the so-called *Ly- α forest*. Its absorption is caused not by individual, confined clouds, but by a gradually varying density field characterized by overdense sheets and filaments and extensive, underdense voids that evolve with time (McQuinn 2016).

1.3. Basic Concepts of Absorption

As light from a distant source propagates to an observer, a fraction can be absorbed via electronic resonance transitions in intervening atoms, ions, or molecules and subsequently reemitted along another path. The specific flux, $F(\nu)$, observed from a background object is expressed in terms of the unabsorbed continuum flux, $F_0(\nu)$:

$$F(\nu) = F_0(\nu)e^{-\tau(\nu)}. \quad 3.$$

At rest frequencies ν corresponding resonance transitions in the intervening gas, the optical depth, $\tau(\nu)$, due to absorption is related to the column density, N , of the absorbing species through

$$\tau(\nu) = \int_0^{+\infty} n\sigma(\nu) ds = N\sigma(\nu), \quad 4.$$

where n is the density of absorbing particles and s is the path through the material. The absorption cross section, $\sigma(\nu)$, is:

$$\sigma(\nu) = \frac{\pi e^2}{m_e c} f\phi(\nu). \quad 5.$$

Here f is the oscillator strength describing the intrinsic strength of the absorption line (a recent tabulation of these “ f -values” can be found in Cashman et al. 2017). The line profile, $\phi(\nu)$, is the intrinsic shape of the absorption line with frequency, itself a convolution of two parts: a central Gaussian core characteristic of the internal motions of the gas and broader Lorentzian wings due to the intrinsic width of atomic energy levels (see Eqn. 6.37 of Draine 2011). For metal line absorption, the central Gaussian component is the most important and is distributed such that $\tau(\nu) \propto \exp(-v^2/b^2)$ for velocity v relative to line center and Doppler parameter b . The Lorentzian wings become important for strong absorption, typically only applicable to H I. An observed spectrum, e.g., Figure 2, is a summation of all of the optical depth profiles – some of which overlap – as convolved by the instrumental line spread function.

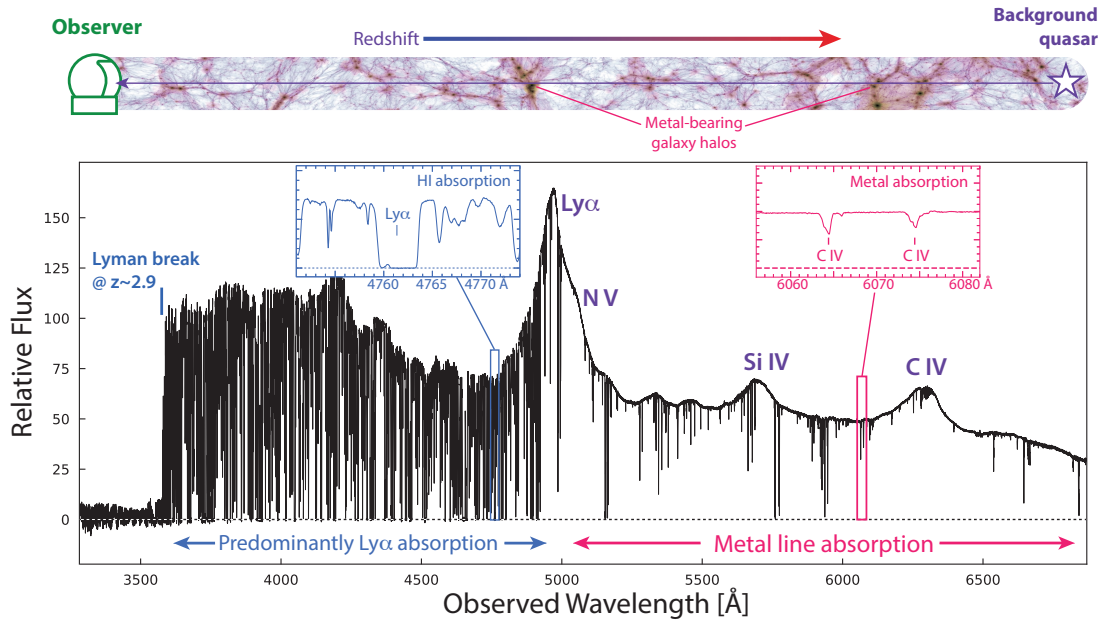


Figure 2

An overview of using absorption line experiments to probe gas in the Universe. *Top:* Light from a background object (in this case a quasar on the right) follows a ray through the Universe toward an observer (left). As the ray passes through the halos of galaxies (the darkest regions in the background image), absorption due to H I and metals is imprinted on the spectrum; additionally, baryonic matter collected into the filaments will also absorb some light, largely in the H I Lyman-series transitions, giving rise to a forest of absorption. *Bottom:* A sample high-resolution spectrum of a high-redshift ($z_{\text{em}} = 3.0932$) quasar recorded at high resolution by UVES on the VLT (D’Odorico et al. 2016). This spectrum has a ultra-high signal-to-noise ratio, $SNR \approx 120$ to 500, with a spectral resolution $R \equiv \lambda/\Delta\lambda \approx 45,000$. Intrinsic emission lines from the quasar are marked across the top. Many redshifted absorption lines are seen in these data. Those at wavelengths longward of the quasar Ly- α emission all arise from metals; those shortward of the Ly- α emission are largely from H I, though with some interloping metal lines. The absorption line profiles encode critical information about the physical state of the gas. The insets show absorption profiles from H I (left) and representative metal lines (right) associated with the $z \sim 2.9$ absorber producing the strong spectral break seen near 3600 Å.

There are three principal approaches to relating the observed line profile to column density (ultimately through Equation 4). The first relies on a measurement of the restframe *equivalent width* of the absorption line, W_{rest} , defined as:

$$W_{\text{rest}} = \int \frac{F_0(\lambda) - F(\lambda)}{F_0(\lambda)} d\lambda_{\text{rest}} = \int (1 - e^{-\tau(\lambda)}) d\lambda_{\text{rest}}, \quad 6.$$

where the restframe wavelength is related to the observed wavelength by the absorber redshift, $\lambda_{\text{rest}} = \lambda_{\text{obs}}/(1+z_{\text{abs}})$. The column density of the absorbing species is then derived from measured equivalent widths by the classical *curve-of-growth* technique (e.g., Draine 2011). The observed equivalent width is not dependent on instrumental resolution, and this technique is useful when several under-resolved lines are available (e.g., using low-resolution spectroscopy).

An alternate approach integrates the *apparent optical depth* of an absorption line to derive its *apparent column density* (Savage & Sembach 1991). The apparent optical depth profile, $\tau_a(v)$, is derived directly from the normalized observed spectrum, inverting Equation

3. The “apparent” here allows for the fact that the observed flux has been convolved by the instrumental line spread function. The apparent column density, per unit velocity, is then

$$N_a(v) = \frac{m_e c}{\pi e^2} \frac{\tau_a(v)}{f \lambda_0} = [3.768 \times 10^{14} \text{ cm}^{-2} (\text{km s}^{-1})^{-1}] \frac{\tau_a(v)}{f \lambda_0(\text{\AA})}, \quad 7.$$

where $\lambda_0(\text{\AA})$ is the central wavelength of the transition (in \AA). The apparent column density is an integration over this $N_a(v)$ profile.

The last approach to deriving column densities is *Voigt profile fitting*, which models the absorption profile based upon the summation of the optical depths from individual absorbing *components*. A comparison of the instrumental line spread function convolved model flux distribution with the observed spectrum constrains three parameters for each component: N , v (the central velocity), and b (the Doppler parameter describing the breadth of its Gaussian core). Ideally, the continuum is also included as a free parameter to the fit. The most important concern of profile fitting is the non-uniqueness of the adopted component model. However, it provides component-by-component physical properties and accounts naturally for saturation when simultaneously using information from multiple transitions of an absorbing species.

Strong neutral hydrogen absorption with $N(\text{H I}) > 10^{19} \text{ cm}^2$ will show *damping wings* in Ly- α due to the Lorentzian component of the optical depth profile. The H I column density is derived by fitting these wings (akin to the profile fitting approach). Such strong absorption is on the *square-root part* of the curve-of-growth, where the equivalent width grows as the square root of the column. The column density of H I can also be derived directly from the equivalent width of Ly- α :

$$N(\text{H I}) = (1.88 \times 10^{18} \text{ cm}^{-2}) \times W_{\text{rest}}^2, \quad 8.$$

where W_{rest} is given in \AA . Note that Lee et al. (2019) discuss departures of the fully quantum mechanical profile from the semi-classical Voigt profile (approximated for a two-level atom) at very high column densities ($N(\text{H I}) > 10^{22} \text{ cm}^{-2}$). Beyond spectroscopy, the cumulative absorption from gas modifies the colors of background sources or provides a frequency-dependent modification of light, providing a means to derive statistical properties of the intervening matter (Prochaska & Zheng 2019; Deharveng et al. 2019).

2. COSMIC EVOLUTION OF BARYONS

Multi-wavelength studies have accurately constrained the growth of galaxies through cosmic time: the rate of star formation per comoving volume peaks at a redshift $z \sim 2$ (the “epoch of galaxy assembly”), stays high up to $z \sim 1$ (Universe age: 2-6 Gyr), then dramatically decreases by more than an order of magnitude from $z \sim 1$ until today (Madau & Dickinson 2014). Probing the fuel for star formation, i.e. the denser phase of the interstellar medium in high-redshift galaxies, is essential to provide insights into the physical processes producing these changes.

2.1. Cosmic Evolution of Neutral Gas

Neutral atomic hydrogen (H I) gas, a primary ingredient for star formation, is therefore a key input to understand how various processes govern galaxy formation and evolution. In this section, we provide a review of recent measurements of the neutral phase of the

gas in the Universe and its evolution with cosmic time. We note that this census is more than an accounting exercise, but rather aims at representing the cosmic cycling of baryons (Fukugita & Peebles 2004; Bouché et al. 2005, 2006, 2007; Shull et al. 2012).

2.1.1. Basic Principles of Characterizing the Neutral Gas Mass Density. The column density distribution function (Figure 1b), the rate of absorber incidence per unit column density per unit absorption path is characterized as:

$$f(N, z) dN dX = \frac{\mathcal{N}}{\Delta N \sum_{i=1}^m \Delta X_i} dN dX, \quad 9.$$

where \mathcal{N} is the number of absorbers observed in a column density bin $[N, N + \Delta N]$ obtained from the observation of m background sources with total absorption distance coverage $\sum_{i=1}^m \Delta X_i$.

The distance interval, ΔX , relates the observed redshift path to co-moving path length; thus, it depends on the geometry of the Universe. In the current preferred flat cosmology (Λ CDM), $X(z)$ is (Bahcall & Spitzer 1969):

$$X(z) = \int_0^z (1+z)^2 \left[\frac{H_0}{H(z)} \right] dz = \int_0^z (1+z)^2 [\Omega_\Lambda + \Omega_m(1+z)^3]^{-1/2} dz, \quad 10.$$

(assuming the curvature term $\Omega_k = 0$, and Ω_Λ is constant with redshift). The comoving baryonic mass density of the gas is computed by integrating the observed column density distribution:

$$\rho_{\text{neutral gas}}(z) = \frac{H_0 \mu m_H}{c} \int_{N_{\min}}^{N_{\max}} N f(N, z) dN, \quad 11.$$

where μ is the mean molecular weight of the gas which is taken to be 1.3 (76% hydrogen and 24% helium by mass), m_H is the hydrogen mass, and N_{\min} and N_{\max} are the bounds of the column density regime being studied. The mass density is commonly expressed relative to the critical mass density at $z=0$, $\rho_{\text{crit},0}$, so that a non-evolving quantity results in a constant value of the density, $\Omega(z)$:

$$\Omega(z) = \rho(z)/\rho_{\text{crit},0} = \rho(z)/(3 H_0^2/8\pi G). \quad 12.$$

Here G is the gravitational constant and H_0 the Hubble constant. For our adopted cosmology, $\rho_{\text{crit},0} = 1.36 \times 10^{11} M_\odot \text{ cMpc}^{-3}$. Note that the comoving mass density we use here is related to the proper mass density by $\rho(z) = \rho_{\text{proper}}(z)/(1+z)^3$.

In practice the integral in Equation 11 is sometimes fitted with multiple power laws for the purpose of integration. These fits may diverge at large column densities, forcing an artificial choice of cut-off (N_{\max} or infinity). The choice can make a substantial difference in the resulting $\Omega_{\text{neutral gas}}$. An alternative is to utilize a 3-parameter Schechter function which converges at high column densities (Péroux et al. 2003; Zafar et al. 2013). The integration of the column density distribution indicates that the lowest column density absorbers dominate by number, while the rare strong systems are major contributors to the total neutral gas density (e.g., Péroux et al. 2003; Noterdaeme et al. 2012). It is a common misconception that such surveys are biased against high column density material due to its relatively small cross section on the sky. Absorption line surveys are ultimately probing the *volume density* by assessing the column density per unit absorption path; they are independent of the spatial distribution of the gas through characterization of the absorber frequency in Equation 9 (see Figure 1b).

Several distinct observational techniques have been used to measure the abundance of neutral hydrogen in the Universe. The approaches change with redshift due to the differences in transitions that are accessible. At $z \lesssim 0.4$, the current generation of radio telescopes measures H I 21-cm emission, which provides a direct estimate of the H I mass. The emission arises from the hyperfine splitting of the ground state of neutral hydrogen into two levels because of the spin-spin interaction between the electron and proton. An electron located in the upper energy level can decay into the lower energy state by emitting a photon with a rest wavelength of ≈ 21 cm or frequency ≈ 1420 MHz. Recent surveys have made robust measures of the local H I mass function and mass density of galaxies (Jones et al. 2018; Westmeier 2018). An integral over these provides a measure of $\Omega_{\text{neutral gas}}$. Observing at higher redshift is challenging as the line is intrinsically faint and because of the increased importance of radio frequency interference at low frequencies. An important goal of the next decade will be to push the 21-cm observations (through stacking or otherwise) to higher redshifts that overlap other observational techniques, notably with SKA pathfinders such as ASKAP and MeerKAT (Curran 2018).

Redshifts above $z \sim 0.4$ are currently beyond the sensitivity of 21-cm searches. Characterization of the H I content at higher redshifts rely on the direct detection of H I Ly- α 1215 Å absorption in the spectra of background quasars. These observations yield direct estimates of $N(\text{H I})$ for neutral gas absorbers through the Ly- α damping wings. At $z \lesssim 1.7$ the Ly- α line is obscured by the Earth’s atmosphere, requiring expensive space-borne ultra-violet (UV) spectroscopy. A combination of the geometry of the Universe and the paucity of absorbers requires sampling many sightlines. Limited blind surveys have been done with HST and other single-object spectroscopic missions. The most statistically robust surveys have made use of preselection of candidate absorbers using strong metal-lines (typically including Mg II) initially observed in ground-based surveys (see Rao et al. 2017).

Over the $1.7 \lesssim z \lesssim 5$ redshift range, the Ly- α transition is observed from the ground; extremely large surveys of thousands of quasar absorbers have brought such studies in a new era (e.g., Noterdaeme et al. 2012; Bird et al. 2017; Parks et al. 2018). These ambitious endeavors with 2.5-m class telescopes – the Sloan Digital Sky Survey, SDSS, in the northern hemisphere and the 2dF quasar survey in the southern hemisphere – advanced the field significantly primarily because they produced homogeneous advanced data products for well over one million low-resolution quasar spectra. In the near future, dedicated spectroscopic surveys on 4-m class telescopes will provide a new wealth of low and medium-resolution quasar spectra in extremely large numbers, notably the WEAVE-QSO survey, the DESI experiment, and surveys with the 4MOST experiment. Clearly, such surveys will require specific approaches to analyse these large data outputs.

At $z \gtrsim 5$, the strong H I absorbers are challenging to identify observationally, as the Ly- α forest becomes highly absorbed. The forest becomes opaque for H I neutral fractions $\geq 10^{-3}$, which provides a blanket of absorption that leaves little continuum against which to search for strong Ly- α absorption. There have been however recent success in measuring the O I forest (Becker et al. 2019) as well as the red damping wing’s effect on the quasar flux (Davies 2019). Higher-resolution quasar spectroscopy with the next generation of extremely large telescopes (e.g. ELT/HIRES, GMT/G-CLEF) will allow us to recover transmission peaks against which neutral absorbers may be measured up to the reionisation redshift (Maiolino et al. 2013). Alternatively, observers will have to rely on other tracers of neutral gas at the highest redshifts.

A promising approach for the future is intensity mapping, which uses low spatial-

resolution surveys of unresolved sources over large cosmological volumes to map overdensities on large scales. Kovetz et al. (2017) summarize current and future intensity mapping experiments. A range of lines will be used to statistically assess the densities of neutral gas traced by 21-cm emission (Chang et al. 2010; Masui et al. 2013) and molecular gas traced by CO (Keating et al. 2015) and [C II] (Pullen et al. 2018) up to the highest redshifts, both from existing observatories and from purpose-built future facilities: e.g. CONCERTO on the APEX telescope and AtLAST.

2.1.2. Neutral Gas Mass Density. Figure 3 shows a collection of $\Omega_{\text{neutral gas}}$ measurements from the literature as crosses. We base this compendium on results from the last decade. Rather than try to be exhaustive, we chose representative results that avoid redundant use of the same datasets. Our compilation at low-redshift ($z \lesssim 0.4$) includes measurements from 21-cm emission surveys and spectral stacking efforts (Delhaize et al. 2013; Rhee et al. 2013; Hoppmann et al. 2015; Rhee et al. 2016; Jones et al. 2018; Rhee et al. 2018; Hu et al. 2019; Bera et al. 2019), although the latter is more prone to confusion issues (see Elson et al. 2019). Our collated results at high redshift include measurements using both high-resolution spectroscopic surveys of tens of objects (Zafar et al. 2013; Crighton et al. 2015; Sánchez-Ramírez et al. 2016; Rao et al. 2017) as well as analyses of lower-resolution spectra of thousands of objects recorded by SDSS (Noterdaeme et al. 2009, 2012). We have homogenized the data to our chosen cosmology and accounted for the contribution from helium, multiplying the H I values by $1/0.76$. We note that 21-cm emission surveys encompass the total H I-mass, while absorption techniques reported here are limited to systems with $\log N(\text{H I}) > 20.3$. Lower column density quasar absorbers contribute an additional 10–20% to the total H I content (Zafar et al. 2013; Berg et al. 2019).

In the absence of a physical motivation which would favour a specific functional form, we fit the cosmological evolution of $\Omega_{\text{neutral gas}}$ with a mathematically simple two-parameter power-law. We derive the best-fit function in $(1+z)$ space:

$$\Omega_{\text{neutral gas}}(z) = [(4.6 \pm 0.2) \times 10^{-4}](1+z)^{0.57 \pm 0.04} \quad 13.$$

The 68% and 95% confidence intervals based on bootstrap estimates are shown in Figure 3. This fit is only appropriate at redshifts for which we currently have data, since at the highest redshifts approaching reionization the neutral gas density approaches the total baryonic density.

The comoving mass density of neutral gas evolves relatively little over time, decreasing as $\propto (1+z)^{0.57}$ from $z \approx 5$ to today. Historically, it was believed that the neutral gas provided all the raw material for the formation of stars, so its redshift evolution should counterbalance the star formation activity over the history of the Universe (Wolfe et al. 1986). The relatively modest evolution throughout cosmic time of the neutral gas density is in contrast to the now well-determined star formation rate density, which rose sharply to a peak at redshifts $z \sim 1-2$ before declining by an order of magnitude to today's modest levels of star formation (Madau & Dickinson 2014). The inset of Figure 3 shows the change in comoving mass density since $z = 5$, $\Delta\rho_5$, following Crighton et al. (2015). The change in comoving stellar mass density is from an integration of the star formation rate density of Madau & Dickinson (2014) (see §3.5.1; we assume 50% uncertainties). The negative change in neutral gas density is based on the power-law fit in the main figure (with 68% confidence interval shaded). At $z < 2.5$, the increase in stellar mass is significantly larger than the neutral gas consumption. These observations call for the global and continuous

Supplementary Material: All of the data used to make the figures presented in this review are available as online supplementary tables.

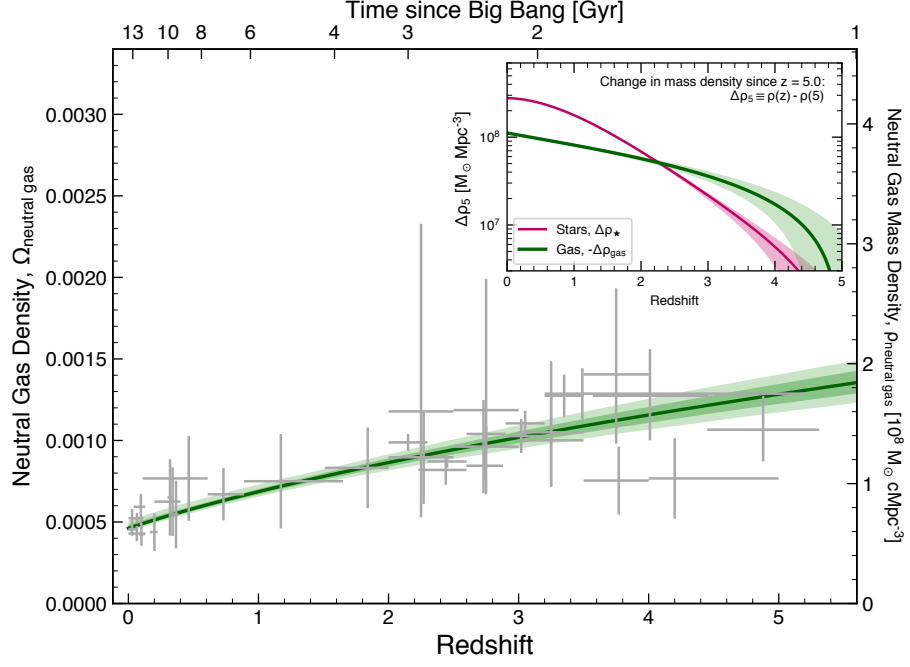


Figure 3

Cosmic evolution of the neutral gas density, $\Omega_{\text{neutral gas}} \equiv \rho_{\text{neutral gas}} / \rho_{\text{crit},0}$. In this and following figures, the corresponding comoving density in mass units, $\rho_{\text{neutral gas}}$, is shown on the right axis. The crosses display the results from individual surveys from the literature. Those at $z \lesssim 0.4$ are from 21-cm emission measurements; the higher redshift values are assessed through Ly- α absorption. The power-law fit described in Equation 13 is shown with the thick line. The gas density is on the whole well determined and shows a mild evolution with cosmic time. *Inset*: The change in comoving gas mass density since $z = 5.0$, $\Delta\rho_5$. By $z \lesssim 2.5$, the total increase in stellar mass density exceeds the neutral gas consumption, requiring replenishment of the neutral gas supply.

replenishment of the neutral gas from the ionized gas reservoir in the intergalactic medium (e.g., Wolfe et al. 2005; Prochaska & Wolfe 2009; Zafar et al. 2013).

From the theoretical viewpoint, the key processes of the production and consumption of the neutral gas have to be introduced into simulations in the form of sub-resolution effective models. For these reasons, simulations of the cold phase of the gas have relied on so-called semi-analytical approaches (Lagos et al. 2011; Davé et al. 2017). More recently, IllustrisTNG simulations (Nelson et al. 2019) in particular have been post-processed to reproduce the cosmological evolution of neutral gas (Diemer et al. 2019). Improved methodology to model the atomic-to-molecular transition on the galaxy-by-galaxy basis (including empirical, simulation-based, and theoretical prescriptions) have been used to compare the cold gas mass function with $z=0$ observations. Reliable predictions will have to await more complete treatment of self-shielding and the full chemistry in higher-resolution cosmological simulations, which to date remain computationally challenging (Richings et al. 2014; Maio

& Tescari 2015; Emerick et al. 2019).

2.2. Cosmic Evolution of Molecular Gas

The molecular phase is at the heart of the physical processes through which gas is converted into stars. Neutral hydrogen provides the essential fuel, but this fuel has to cool and transform to the molecular phase for star formation. It is now possible to constrain the molecular content of large sample of galaxies (Saintonge et al. 2011; Tacconi et al. 2020). The first unbiased survey for molecular gas done through a blind scan was by Walter et al. (2014). An analogous blind survey, ASPECS, has been done in ALMA 3 and 1 mm (respectively ~ 100 and 250 GHz) bands in the Hubble Ultra Deep Field (UDF, Decarli et al. 2016, 2019). ASPECS is the first assessment of the cosmic evolution of molecular gas to $z < 4$; the results are subject to significant uncertainties due to small number statistics and the impact of cosmic variance. In addition, the VLA-based COLDz survey made complementary measurements at $z > 4$ (Riechers et al. 2019), while the IRAM 30m-based xCOLD GASS provided robust $z=0$ measurements (Saintonge et al. 2017). Figure 4 illustrates our current knowledge of the cosmic evolution of the molecular gas from these surveys. We note that CO absorption provides an alternate approach to assessing $\Omega_{\text{molecular gas}}$; Klitsch et al. (2019a) use the ALMA calibrator archive to search for absorption, providing stringent limits on the molecular gas density at $z < 1.5$ based on non-detections of CO. This approach is promising as it allows to reach lower gas column density free from cosmic variance issues (see also Kanekar et al. 2014).

The molecular measurements reported here arise from studies undertaken in just the last few years, we expect that observational determination of $\Omega_{\text{molecular gas}}$ will make rapid progress in the decades to come. In addition to improve sample size and observation depth, there are some limiting systematic issues in using CO as a tracer of molecular gas that will require a better theoretical understanding to improve. The limited simultaneous frequency coverage (bandwidth) of current receiver arrays produce a redshift-transition degeneracy inherent to single-line detections. Moreover, the observed higher rotational quantum number transitions require a conversion to the reference CO(1–0). This step introduces an uncertainty due to variation in poorly known Spectral Line Energy Distribution (SLED) of different galaxy types (Carilli & Walter 2013; Klitsch et al. 2019b). The CO-to-H₂ conversion factor adds a large systematic uncertainty, as well. Indeed, CO likely breaks down as a reliable tracer for H₂ mass in extreme environments. In particular, the conversion factor transforming CO intensity to H₂ mass increases with decreasing metallicities as CO photodissociates to a larger depth in each cloud, and as a result varies both from object to object as well as with redshift (e.g. Bolatto et al. 2013). Other tracers may eventually provide feasible substitutes for CO searches, such as [C I] and [C II] (Papastergis et al. 2012). In principle, the direct measurement of resonant electronic Lyman and Werner bands of H₂ in absorption at UV-wavelengths in H I absorbers (found in $\sim 4\%$ of absorbers; Bolmer et al. 2019) could be used to explore the scalings between CO, C I, and H₂ (Noterdaeme et al. 2018).

On the theoretical side, the molecular phase of the cold gas is challenging to model because of the complex unknown physics involved. In addition, modelling below the hydrodynamic simulation’s resolution (coined “sub-grid” modelling) is required to capture this phase of the gas. Simple semi-analytical techniques based on metallicity and pressure-based models (Krumholz 2013, and references therein) are used to split the cold hydrogen from

hydrodynamics simulations (such as EAGLE or Illustris) into its atomic and molecular components (Lagos et al. 2015; Popping et al. 2019). Simulating the neutral and molecular phases of the cold gas in full cosmological context is therefore one of the most crucial and challenging objective of studies of galaxy formation and evolution in the decades to come.

2.3. Cosmic Evolution of Condensed Matter

Having summarized the densities of cold gas, including the neutral (§2.1.2) and molecular (§2.2) components, we combine these with measurements of the stellar mass density to study the transitions between these baryonic components of the Universe. We refer to these components collectively as *condensed* matter. Our goal is to assess the baryon inventory of condensed material and its cosmic evolution over a look-back time of ~ 13 Gyr. Building on previous works that have performed such accounting exercises (e.g. Pettini 1999; Fukugita & Peebles 2004; Bouché et al. 2007; Shull et al. 2012), we here present the change of the different components with time as gas is converted into stars (Putman 2017; Driver et al. 2018).

Understanding the efficiency with which baryons are converted into stars is a challenge in studies of galaxy formation and evolution. The evolution in the star formation rate density is well established from observations of star-forming galaxies across cosmic time at infrared, ultra violet, submillimetre, and radio wavelengths (Madau & Dickinson 2014). The star-formation rate (SFR) density increased at early times, reached a peak at around $z \sim 2$, and subsequently decreased through today. Identifying the physical processes that drive this dramatic change and their relative importance are active areas of current research.

Figure 4 summarises the observable quantities making up the baryon content of the “condensed” phases of the Universe, those collected into high density regions. At the top of the plot, the horizontal line indicates the total baryon density of the Universe. Both measurements of CMB anisotropies (Planck Collaboration et al. 2016) and light element abundances coupled with Big Bang nucleosynthesis (Cooke et al. 2018) lead to $\Omega_{\text{baryons}} \approx 0.0455$ (in our adopted cosmology). The fact that these two independent measures from vastly different physical processes occurring at enormously different cosmic ages agree to within $2\text{-}\sigma$ is a real triumph of cosmology. The mass in stars is well constrained from measurements of the stellar mass density (§3.5.1), and it is found to build up steeply with redshift. The neutral phase of the gas has also been well constrained in recent years; we show the fit to the data from Figure 3, indicating a steadily decreasing density with cosmic time (§2.1.2). We also plot the molecular gas density from the blind CO emission line surveys discussed in §2.2.

Globally, Figure 4 shows the neutral gas density dominates the molecular gas density at all redshifts. This differs from the assumptions on galaxy scales of Tacconi et al. (2018), who argue that neutral gas in high redshift galaxies is negligible (see Tacconi et al. 2020). The molecular gas and stellar components have similar densities until $z \sim 2$, after which the molecular gas density decreases rapidly, while the stellar mass of the Universe continues to increase. Overall, the shape of the molecular mass density mirrors that of the star formation rate density of the Universe (Decarli et al. 2019; Tacconi et al. 2020). Our findings indicate that the history of star formations rates is primarily driven by the cosmic evolution of the gas reservoir.

In this review, we elected to focus on the densest baryons (the condensed matter in our nomenclature); these are the most strongly coupled to star formation within galaxies

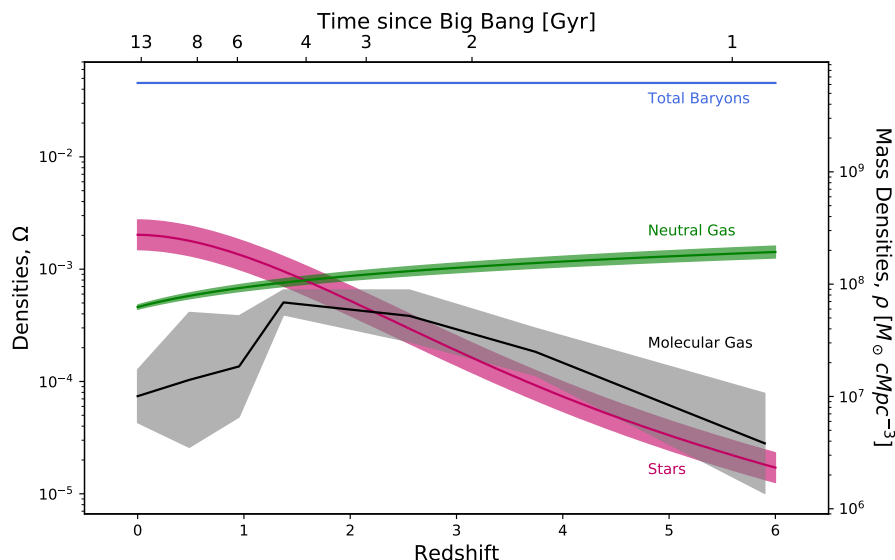


Figure 4

Cosmic evolution of the density in condensed matter (stars, neutral gas, molecular gas). The total baryonic density of the Universe estimated from CMB anisotropies and from light element abundances is shown at the top. The condensed forms of the baryons illustrate the cycling of baryons most closely contributing to the make-up of galaxies. At all redshifts the neutral gas density dominates over that of the molecular gas. The molecular gas density evolution roughly mirrors that of the star formation rate density (Madau & Dickinson 2014), hinting that the molecular gas reservoir drives the evolution of star formation.

and are the most robustly observed. Naturally there are a number of other contributors to the baryon budget which are either challenging to probe observationally and are not included in Figure 4. At high-redshift, cosmological hydrodynamical simulations indicate most of these baryons are in the low-density ionized gas of the Ly- α forest, for which deriving the density from observations is highly model-dependent. At lower redshifts, a larger fraction of baryons are collected on the galaxy halo scale, including in the CGM (Werk et al. 2013; Tumlinson et al. 2017). A major fraction of the baryons at lower redshift is found in hot gas (10^5 - 10^6 K), including the gas in groups and clusters as well as the warm-hot intergalactic medium (WHIM; Cen & Ostriker 1999; Davé et al. 2001). This gas can be probed in X-ray experiments and more recently through the distortions the gas imprints on the CMB spectrum due to thermal and bulk motions of free electrons (the thermal and kinetic Sunyaev-Zel'dovich effects; Lim et al. 2018; de Graaff et al. 2019; Tanimura et al. 2019).

We can use the combined masses of the neutral (§2.1.2) and molecular gas (§2.2) to trace the conversion of gas into stars over cosmic time. In the broadest terms, H I clouds form, and these molecular clouds then cool, fragment, and initiate star formation in galaxies. Thus, the cold gas (neutral+molecular) is expected to provide the reservoir of fuel for star formation activity. Figure 5 provides a cumulative view of the observed densities of these dense baryonic phases. Focusing on the total, we note an increase in the combined density

with time, indicating that the cold gas reservoir at early times is insufficient to provide for all of the stellar and cold gas content seen today (comparing the sum at lower redshift with the dashed line denoting the value seen at the highest redshifts). At $z \gtrsim 2.5$, the total density of condensed matter is relatively constant; we see the conversion of H I into H₂ and stellar mass. However, at lower redshifts the H I is rapidly depleted into molecular gas, while the stellar mass density grows at an even higher pace. At $z \leq 2.5$, the combined neutral and molecular gas densities decrease strongly, though the total mass in condensed matter grows, reaching nearly twice its value at the highest redshifts. This requires a continues conversion of other forms of matter into these condensed forms in order to provide for the overall growth.

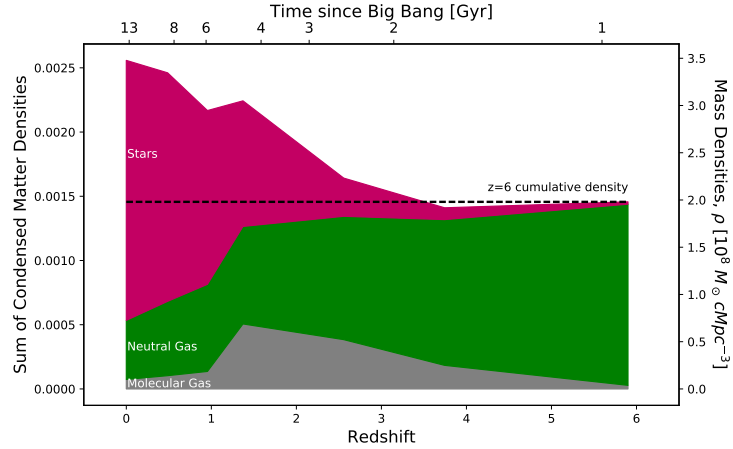


Figure 5

Cumulative view of the redshift evolution of the total density of condensed matter: summing the molecular gas, neutral gas, and stars. At $z > 3$, we witness the formation of H₂ gas from H I resulting in a constant amount of condensed matter (horizontal dashed line). At $z < 3$, the amount of neutral gas decreases and the molecular gas is rapidly consumed into star formation.

A measure of the rate of gas conversion into stellar mass is the gas depletion timescale, the time that would be required to convert the gas into stars at the current rate. It is expressed as:

$$\tau_{\text{dep}} = \rho_{\text{gas}} / \dot{\rho}_{\star}, \quad 14.$$

where $\dot{\rho}_{\star}$ is the star formation rate density. τ_{dep} is therefore related to the Kennicutt-Schmidt relation (Kennicutt 1998). The inverse of τ_{dep} is often defined as the star formation efficiency, $\text{SFE} = 1/\tau_{\text{dep}}$, even though it is related to a rate, expressed in units of yr^{-1} . Figure 6 presents a comparison of the molecular and cold (neutral+molecular) gas depletion timescales as function of redshift. The allowed values of the depletion time range from $\tau_{\text{dep}} = 100$ Myr to 1.5 Gyr, in line with previous findings (Saintonge et al. 2017; Tacconi et al. 2018; Riechers et al. 2019). τ_{dep} is roughly constant with redshift, within the sizeable uncertainties (denoted by the filled area in Figure 6). Tacconi et al. (2020) find a mild redshift evolution in τ_{dep} measured in massive galaxies, proportional to $(1+z)^{-1}$ (dashed-dotted line in Figure 6). While coming from different approaches (measurements of the global quantities of baryons in the Universe versus in-situ observations targetting galaxies), the two results are remarkably

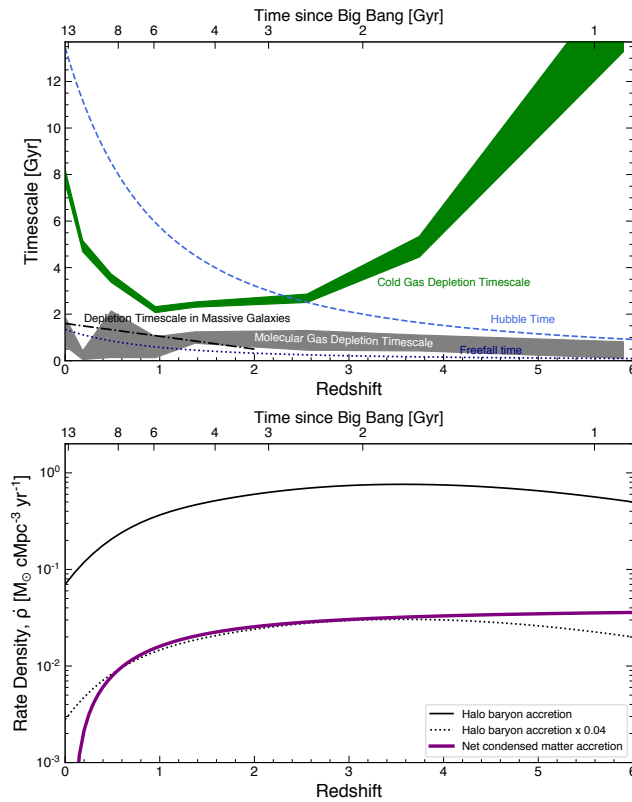


Figure 6

Top: Timescales for conversion of gas in its various forms to stars at each redshift. The filled areas show the depletion timescales of the molecular or cold gas. The molecular gas depletion scale shows a constant value with redshift, whereas the cold gas depletion time (inclusive of molecular and neutral gas) varies significantly with redshift. The dot-dashed line shows the functional fit to the molecular depletion timescale measured in a sample of massive galaxies by Tacconi et al. (2020), which is in agreement with our global estimate. The cold gas depletion times are shorter than the dynamical time (taken to be 10% of Hubble time), implying the need for conversion of ionized gas from the circumgalactic medium and/or intergalactic medium to supply additional fuel for star formation. At $z \lesssim 1$, the molecular gas consumption time is comparable with the dynamical time, implying the reservoir of molecular gas is slowly becoming insufficient to fuel the observed star formation. Bottom: The purple line shows the net accretion rate density required to reproduce the observed evolution of the mass density in condensed matter (Figure 5). Also plotted is the baryonic accretion rate onto halos as a function of redshift. In addition, we show the baryonic accretion rate density scaled by an efficiency 0.04 for conversion of accreted baryons into condensed matter, showing the similarity between the shape of the accretion rates that are continuously decreasing with time, dropping significantly at $z < 1.5$. Together, these results indicate that globally the growth of condensed matter (stars and cold gas) in the Universe scales principally with the dark matter accretion rate onto halos. The gas regulator model, in which star formation in galaxies is instantaneously regulated by the mass of the gas reservoir (e.g., Bouché et al. 2010; Lilly et al. 2013), is in remarkable agreement with this global picture of a continual cycle of baryons flowing in and out of galaxies as a key moderator of galaxy evolution.

consistent. It confirms that globally the molecular gas depletion timescale depends weakly on stellar mass, which is consistent with recent observations at low redshifts (e.g., Tacconi et al. 2018). The steady timescale for global molecular gas depletion over ~ 13 Gyr lookback time points toward a fundamental and universal physical process of conversion of molecular gas into stars. This is in contrast to τ_{dep} for cold gas (neutral+molecular), which is large at high redshifts. We compare these values to the typical dynamical time for halos in Figure 6, which is roughly $\sim 10\%$ of the Hubble time (Lilly et al. 2013; Tacconi et al. 2020). We note that the cold (neutral+molecular) gas depletion timescale is much longer than the dynamical time at all redshifts, indicating that the reservoir of cold gas is sufficient to sustain the rate of star formation for many dynamical times at all epochs. At $z \lesssim 1$, the molecular gas consumption time is comparable to the dynamical time, implying the reservoir of molecular gas is slowly becoming insufficient to fuel the observed star formation. There is a large reservoir of cold gas at these redshifts, but the efficiency with which it is converted into molecular gas is low.

The increase in the cumulative mass densities of cold gas and stars with decreasing redshift calls for the intake of new material into condensed matter. From this we infer the *required* rate of transformation to reproduce the rise in total condensed matter. This is the result of the *net* conversion of ionized gas from the CGM and IGM reservoirs into cold gas and stars (e.g., Wolfe et al. 2005; Prochaska & Wolfe 2009; Bauermeister et al. 2010; Zafar et al. 2013). This is inclusive of recycling material on galactic scales, with some material previously ejected and ionized by feedback returning to the condensed phases. We plot this net rate of conversion of ionized gas into the condensed phase per unit volume in Figure 6. The net accretion rate density continuously declines with cosmic time. Also plotted is the baryonic accretion rate onto halos as a function of redshift. We calculate the total mass accretion as the virial mass growth rate of halos from Dekel & Burkert (2013) integrated over the Bocquet et al. (2016) mass functions at each redshift. The baryon mass accretion rate is the total matter accretion rate scaled by the cosmic baryon fraction ($\Omega_b/\Omega_m = 0.15$ in our adopted cosmology). The baryon and net condensed matter accretion rates have similar shapes; both are high until $z \sim 1.5$ and then drop significantly through today. The drop in accretion rate at low redshift is caused in part by the expansion of the Universe as galaxies are driven away from each other by the repulsive force of dark energy; accretion and merging is slowed, and galaxies are gradually starved of incoming fuel. This accretion rate includes the effects of both smooth accretion and mergers, whose mix changes with redshift and halo mass (Padmanabhan & Loeb 2020). We also plot in Figure 6 the baryonic accretion rate density scaled by an efficiency of 0.04 for conversion of accreted baryons into condensed matter, showing the similarity between the shape of the accretion rates. These similarities point to a causal relation between dark matter accretion and the rate of growth of condensed matter. This efficiency describes the conversion of accreted baryons into condensed matter for material accreting onto all halos—including cluster scales. The low efficiency rate implies that a majority of the new baryons accreted into halos are in ionized forms, both warm photoionized material and hot coronal gas. There are several reasons for this. Gas being accreted onto halos from the IGM has a low-enough density that it is necessarily ionized. Furthermore, the accretion process involves shocks that heat the incoming gas significantly, especially as matter is accreted onto massive galaxies, groups, and clusters. At the same time, we are comparing the baryon accretion rate with the net rate of growth of condensed matter. The effects of feedback and galactic winds will be to convert some of the cold gas into ionized material. Even given all of these baryonic

processes, globally the growth of condensed matter (stars and cold gas) in the Universe scales principally with the dark matter accretion rate onto halos. These results indicate that the $z < 2$ decline of the star-formation history is driven by the lack of molecular gas supply due to a drop in net gas accretion rate, which is itself driven by a decrease in the dark matter halos accretion rate. At early times ($z \gtrsim 2$), the global SFR density of the Universe increases as the baryon net accretion rate stays high. At late times, the gas reservoir depletes as the accretion rate significantly decreases, and galaxies are quenched. These results are in line with expectations from the gas regulator (or bathtub) model (e.g., Bouché et al. 2010; Davé et al. 2012; Lilly et al. 2013), which uses continuity equations to describe the cycling of baryons in and out of galaxies. The regulator model describes galaxies as systems in a slowly evolving equilibrium between inflow, outflow, and star formation. At early times, galaxies build up baryonic matter during an epoch of gas accumulation, in which the SFR is limited by the available reservoir of cold gas. At later times, galaxies reach a steady state in which global star formation is regulated by the net accretion rate. Given its simplicity, this gas regulator model is in remarkable agreement with the global picture presented in Figure 6, in which the continual cycle of baryons flowing in and out of galaxies is a key moderator of galaxy evolution. (See the sidebar titled Cosmic Evolution of Baryons.)

Cosmic Evolution of Baryons

A modern census of $\Omega_{\text{neutral gas}}$ indicates that the cosmic evolution of H I is now observationally well constrained. Results indicate a mild evolution with a decrease proportional to $(1+z)^{0.57}$. It will be important that 21-cm emission measurements reach the epoch where Ly- α absorption measurements against background quasars are also available to allow for a direct comparison of these two vastly different observing methods. Intensity mapping provides a promising avenue to further push these measurements to the highest redshifts.

While still in their infancy, new measurements of $\Omega_{\text{molecular gas}}$ allow us to make a global assessment of the condensed matter (cold gas and stars) in the Universe from direct observables. At $z > 2.5$, the formation of H₂ from H I results in a nearly constant amount of cold gas. At lower redshift, H₂ decreases rapidly, following the trend in star formation rate. The H₂ depletion timescale is constant with redshift, suggesting a universal physical process of conversion of molecular gas into stars on global scales. At $z \lesssim 1$, the molecular gas consumption time is comparable with the dynamical time, implying the reservoir of molecular gas is slowly becoming insufficient to fuel the observed star formation. At $z \lesssim 3$, the increase in the total density of condensed material requires accretion of the ionized phase of the gas from the CGM and/or IGM baryon reservoir.

We find that the baryonic accretion rate density onto dark matter halos scaled by an efficiency factor of 0.04 shows similarity with the shape of the net condensed matter accretion rate, which are continuously decreasing with time and dropping significantly at low redshift. These results indicate that the $z < 2$ decline of the star-formation history is driven by the lack of molecular gas supply due to a drop in net gas accretion rate, which is itself driven by the decreased growth of the dark matter halos. These observations are in remarkable agreement with the gas regulator model, which describes a continual cycle of baryons flowing in and out of galaxies as a key moderator of galaxy evolution.

3. COSMIC EVOLUTION OF METALS

The detection of cosmic matter through absorption lines is also key to trace the metallicity evolution of the Universe. This is done by measuring absorption from metal lines arising in the same gas used to trace the hydrogen gas content of the Universe (e.g., §2.1.2). Using absorption against background sources allows us to assess the metallicity evolution of the Universe with similar sensitivity over $0 \lesssim z \lesssim 5$; it provides a measure of the metallicity weighted by the total gas mass of the Universe rather than by stellar luminosity, as do most metal tracers (stars and H II regions). Absorption line-based metallicities are independent of excitation conditions – they are largely insensitive to density or temperature and require no local source of excitation. This differs from emission line metallicity estimates, where density and temperature information is critical to making high-quality measurements (see e.g. Maiolino & Mannucci 2019; Kewley et al. 2019). The empirical calibrations used to circumvent the need for physical conditions for most studies yield disparate results (Kewley & Ellison 2008). Absorption lines, on the other hand, probe low- and high-metallicity as well as low- and high-excitation regions independently of galaxy stellar masses. In this section, we review the modern estimates of metallicity in various environment and make a census of the total amount of metals in the Universe.

3.1. Basic Principles of Measuring Metallicity through Absorption Lines

The *metallicity* of astrophysical matter summarizes the abundance of metals (elements greater than helium) present relative to hydrogen by number; we express the logarithmic abundance relative to solar of a specific element X as

$$[X/H] = \log\{N(X)/N(H)\} - \log\{N(X)/N(H)\}_{\odot}, \quad 15.$$

where $N(X)$ refers to the column density (surface density in atoms cm^{-2}) of that element, and $\{N(X)/N(H)\}_{\odot}$ is the reference abundance in the Solar System. Throughout this review we adopt the Solar System abundances summarized in Asplund et al. (2009).

Thus the metallicity $[X/H]$ is the logarithmic abundance relative to the assumed solar abundance. When probing regions dominated by neutral gas, the measurements probe the dominant ionization states of X and H, which implies assuming

$$N(X) = N(X \text{ II}) \text{ and } N(H) = N(H \text{ I}). \quad 16.$$

There are important exceptions, e.g., the dominant ionization phases are the neutral states for N and O. Similarly, one calculates relative abundances of metals, e.g., $[X/Y]$. This comparison provides insight into the relative nucleosynthetic contributions of the elements (e.g., §3.2.1) and depletion of the elements into the solid phase (dust; §3.2.2).

3.2. Challenges in Assessing Metallicity

Absorption line techniques provide a means of tracing the cosmic metal evolution. The column densities of the gas is measured with high precision. For ionized and partially-ionized gas, the precision of the derived metallicities is limited by the need for ionization corrections (§3.2.1). In all absorbers, it is also affected by dust depletion (§3.2.2) and dust sample bias (§3.2.3). The details of these effects and corrections to account for them are discussed below.

Logarithmic abundances relative to the Solar System:

[X/H]: abundance of a specific element X

[M/H]: abundance of all metals M

3.2.1. Ionization Effects: Accounting for Differential Ionization. The gas traced by absorption lines is often multi-phased, with sight lines passing through regions of differing temperature, density, and ionization conditions. Observations measure atomic hydrogen and a fraction of the metal ionic states. The presence of gas with neutral H fractions significantly less than unity requires ionization corrections to transform a measured ratio of ionic to H I column density $N(X^i)/N(\text{H}^0)$ into X/H . Methodologically, we write the abundance X/H as

$$\frac{X}{\text{H}} = \frac{N(X^i)}{N(\text{H}^0)} \frac{x(\text{H}^0)}{x(X^i)}, \quad 17.$$

where $x(X^i) \equiv N(X^i)/N(X_{\text{total}})$ is the ionization fraction of X^i and the ratio of ionization fractions in the last term is the *ionization correction factor*, $\text{ICF}(X^i) \equiv x(\text{H}^0)/x(X^i)$. Even systems with high ionization fractions can have $\text{ICF}(X^i) \approx 1$ for specific choices of X^i . The ionization corrections range from unimportant to more than an order of magnitude in partially-ionized (Quiret et al. 2016) and ionized gas (Fumagalli et al. 2016; Wotta et al. 2019). Ionization corrections are negligible in strongly-neutral regions (typically with $\log N(\text{H I}) \gtrsim 20.3$; Vladilo et al. 2001) with the exception of a few atomic or ionic species typically observed only in the densest gas (e.g., C I, Na I, Ca II).

The models used to estimate ICFs employ sophisticated atomic physics and radiative transfer algorithms. Most ICFs are estimated using the plasma simulation code Cloudy (most recently described by Ferland et al. 2017), assessing the ionization in one dimension, assuming a ionizing radiation field incident on a plane-parallel slab of constant density gas.

Advances in the fidelity of such modeling will address the simplifying assumptions currently being made. The radiation field is commonly based on a model of the extragalactic ultraviolet background (UVB) derived from the transfer of radiation from QSOs and star forming galaxies (with an assumed escape fraction) over redshift (Haardt & Madau 2012; Khaire & Srianand 2019; Faucher-Giguère 2019). Background radiation fields with a larger contribution from escaping stellar radiation tend to produce lower abundances (by $\sim 0.3 - 0.5$ dex for several widely-used radiation fields; Fumagalli et al. 2016; Chen et al. 2017; Wotta et al. 2019). The contribution from local radiation sources (e.g., nearby galaxies) can be included, but this typically requires making poorly-constrained decisions about their relative contribution. Given these uncertainties, statistically robust constraints on ICFs will likely come from studies of populations using large samples (e.g., Fumagalli et al. 2016; Wotta et al. 2019), folding uncertainties in radiation field into the assessment of abundance uncertainties. Exploring the ionization of more realistic 3-dimensional geometries, perhaps drawn from hydrodynamic simulations, will also help clarify the uncertainties caused by the simplifying assumptions that are currently made when calculating ICFs.

3.2.2. Dust Effects: Elemental Depletion. It is well-established that most metals are under-abundant in the interstellar gas of the Milky Way and that this deficit is a result of the metals' incorporation into the solid phase, i.e., into interstellar dust. This *depletion* of metals is differential, (Jenkins 2009), with some elements showing a higher affinity for incorporation into solid-phase grains than others based on their chemical properties. In total more than 50% of the metals in the Milky Way's interstellar medium (ISM) are incorporated into grains. Depletion of gas-phase metal abundances are clearly also seen in the Large (De Cia 2018) and Small (Jenkins & Wallerstein 2017) Magellanic Clouds, though with a smaller degree of depletion reflecting the lower dust-to-metals mass ratios in these systems.

Given the presence of dust in a broad range of galaxies, depletion is naturally expected

to be also detected in the material traced by high-redshift absorption lines. Indeed, some commonly-accessible elements can be subject to large biases: 90-99% of the Milky Way’s interstellar Fe is locked into the solid phase (Jenkins 2009), a bias of > 1 dex in the gas-phase abundance compared with the total. There is strong evidence for the differential depletion of metals in the neutral absorbers, though typically to a smaller degree than in the Milky Way (De Cia et al. 2016). Detections of the 2175 Å absorption “bump” (Junkkarinen et al. 2004) and strong infrared absorption features (Aller et al. 2014) associated with solid-phase material at the redshifts of foreground neutral absorbers provide further support for the presence of dust in these systems.

The differential nature of elemental depletion is also an advantage. Early works often used only lightly-depleted elements to derive abundances (e.g., focusing on Zn or to a lesser degree Si). More recent works have taken advantage of the patterns of differential depletion to correct *gas-phase* measurements to *total* metal abundances (e.g., for neutral gas see De Cia et al. 2016, 2018; for partially-ionized gas Quiret et al. 2016; Fumagalli et al. 2016). These efforts follow the spirit of Jenkins (2009), using empirically-calibrated sequences of relative metal depletions to correct for the metals incorporated into grains (De Cia et al. 2016; Jenkins & Wallerstein 2017; De Cia et al. 2018; De Cia 2018).

3.2.3. Dust Effects: Sample Bias. Dusty intervening quasar absorbers can prevent the inclusion of the background quasars from optically-selected samples in the first place. The reddening due to the dust potentially removes the quasars from color-selected samples or the extinction causes them to be too faint to be selected. While analysis of optically-selected quasars provides mixed results on the significance of reddening by absorbers (Frank & Péroux 2010; Murphy & Bernet 2016), there exist examples of quasars outside of these selection criteria that show reddening by high column density foreground absorbers (Geier et al. 2019).

Quantifying the bias introduced by the optical selection requires alternate approaches to identify quasars. Samples of red quasars selected in UKIDSS or mid-infrared WISE appear to be reddened by material intrinsic to the quasars themselves (e.g., Maddox et al. 2012; Krogager et al. 2016). Ellison et al. (2001) were the first to use a radio-selected quasar sample of ≈ 25 objects to characterize the differences with optically-selected samples, finding no significant discrepancies in the absorber statistics. Jorgenson et al. (2006) found a similar result using a larger radio-selected sample; however, they did identify eight candidate radio quasars (out of their sample of ~ 60) with no optical counterparts down to faint limits, hence possible candidates for lines of sight with dusty absorbers. These samples likely remain too small to put strong constraints on the presence of high column density, high metal/dust-content absorbers.

Vladilo & Péroux (2005) use the Galactic extinction law to estimate that while the dust content of observed absorbers is not high, systems at $z = 1.8\text{--}3.0$ with higher metal and dust columns than found in the current sample may be responsible for obscuring $\approx 30\%$ to 50% of quasars. In this case, the highest metal content absorbers are missing from any census, thus significantly biasing our results. Work by Krogager et al. (2019) also including the effect of color selection argues that current quasar samples possibly underestimate the mass and metal densities of absorbers by at least 10–50% and 30–200%, respectively. To progress on quantifying this effect directly, promising alternate paths include quasar selection via luminosity variability (Palanque-Delabrouille et al. 2016) – especially in the LSST era, X-ray selected (Merloni et al. 2012), or the absence of proper motions in astrometric surveys

(e.g., with the *GAIA* mission; Heintz et al. 2018).

3.3. Building Statistical Samples of Cosmic Metals

Samples of high quality quasar spectra key to measuring gas-phase metals have expanded dramatically in the last two decades thanks in parts to opportunities offered by high-resolution spectrographs on 8–10 m-class telescopes. Publicly available archives of quasars are providing an unprecedented new pool of hundreds of quasar spectra up to the highest spectral resolution ($R > 40,000$). Homogeneous reprocessing of such datasets provides a goldmine to address new science goals beyond those of the initial observers for both ground-based (Zafar et al. 2013; Murphy et al. 2019; O’Meara et al. 2017)² and space-based data (Peeples et al. 2017).³ This approach extends to mm wavelengths, with ALMACAL⁴ providing access to a large sample of quasar sight lines (Klitsch et al. 2019a). We anticipate that this ultimate part of the data flow, making science-ready data publicly available, will become a key component of observatories in the future.

3.4. Cosmic Evolution of Neutral Gas Metallicity

We present here a collection of depletion-corrected total metallicity measurements of neutral gas ($\log N(\text{H I}) \geq 20.3$). This compendium provides a measure of the global mean metallicity from $z \approx 5$ to today. Figure 7 shows the metallicities of a select sample of neutral gas absorbers as a function of redshift. Here we use $[\text{M}/\text{H}]$ to signify the generic metallicity. Functionally we adopt $[\text{M}/\text{H}] = [\text{Si}/\text{H}]$ to tie the metallicity to α elements. Readers should be aware that the non-solar α/Fe ratios in low-metallicity absorbers can make this depart from $[\text{Fe}/\text{H}]$. However, we find that the $[\text{M}/\text{H}]$ values presented here are close proxies for the abundances by mass (i.e., $Z_{\text{neutral gas}} \approx Z_{\odot} \times 10^{[\text{M}/\text{H}]}$). Along the right axis we show the corresponding $12 + \log(\text{O}/\text{H})$ scale favored in H II region emission line metallicity studies. H II region metallicity determinations probe a different phase of the ISM than the data shown here and are likely affected by self enrichment. Studies comparing neutral and ionized gas metallicities in the same galaxies find they are in good agreement (Christensen et al. 2014; Rahmani et al. 2016).

The majority of the measurements in Figure 7 are drawn from the dust-corrected sample compiled by De Cia et al. (2018).⁵ The individual $[\text{M}/\text{H}]$ measurements are listed in Supplemental Table 1. The correction for elements locked into dust grains is based on the measurement of the relative amounts of multiple elements, with reference to empirical calibrations using the Milky Way, Magellanic Clouds, and neutral absorbers (De Cia et al. 2016,

²UVES/SQUAD: https://github.com/MTMurphy77/UVES_SQUAD_DR1,
HIRES/KODIAQ: <https://koa.ipac.caltech.edu/applications/KODIAQ/kodiaqDocument.html>

³HST/COS: https://archive.stsci.edu/hst/spectral_legacy/

⁴ALMA: <https://www.almacal.wordpress.com>

⁵Specifically, we included all systems in Table C2 of De Cia et al. (2018). In cases where there were duplications with Table C2, we favoured the values listed in Table C1. We added two objects present in Table C1 but not in Table C2 (namely J1009+0731 and Q0454+039) and removed two systems which are formally below the DLA canonical definition (J1237+0647 and Q0824+1302). We have complemented the De Cia et al. sample with additional measurements at $z \gtrsim 4$ from the compilations of Berg et al. (2016) and Poudel et al. (2018) as well as at $z \lesssim 1$ drawing from Oliveira et al. (2014) and the compilation of Wotta et al. (2016). For these complementary systems, we have derived dust-corrected metallicities following De Cia et al. (2018).

2018). This approach corrects for the differential elemental depletion into dust, providing the total gas+dust abundance of the neutral absorbers in Figure 7. Making corrections for differential depletion requires measurements of more than one metal. This sample, through this requirement, leaves off some of the highest-redshift metallicity measurements, leading to a limited number of systems at $z > 4.5$. Figure 7 shows a general trend of increasing metallicity with decreasing redshift, reaching nearly solar metallicity today. We also note that the scatter of the individual measurements is larger than rise with cosmic time.

We note that the sample presented in Figure 7 is not sensitivity limited. We show in dashed horizontal lines the limits of metallicity measurements over two redshift regimes corresponding to the ultraviolet and optical wavelength windows which are below the lowest data in our compilation. Our compendium, which is designed to trace the mean metallicity of the entire population, intentionally excludes results from specialized searches for low-metallicity gas (e.g., the $[M/H] \sim -3.2$ system identified by Cooke et al. 2017). Indeed, beyond using metal tracers, a quest has been undertaken to identify the chemical signature of the first stars among the most metal-poor quasar absorbers (see recent work by Cooke et al. 2017, and references therein). Identifying and measuring the detailed chemical abundance patterns of the most metal-poor absorbers is important to determine the chemical abundance pattern of the earliest generation of stars and perform a strong and informative test of nucleosynthesis models of metal-free stars. Future prospects of finding extremely metal-poor (and possibly pristine) gas at high redshift are promising with the next generation of telescopes (Fumagalli et al. 2011; Cooke et al. 2017).

Figure 7 also shows the H I-weighted mean metallicity as large dots with error bars. The H I-weighted mean metallicity provides a robust measure of the global metallicity evolution of the neutral phase of the Universe. We compute column density-weighted mean abundances of n systems in each redshift bin as:

$$[\langle M/H \rangle] = \log \langle M/H \rangle - \log (M/H)_\odot \quad 18.$$

where

$$\langle M/H \rangle \equiv \frac{\sum_{i=1}^n 10^{[M/H]_i} N(H\text{ I})_i}{\sum_{i=1}^n N(H\text{ I})_i} \quad 19.$$

The resulting values are shown in the Figure 7 and summarized in Table 1. The horizontal errors show the bin size, while the data points are located at the H I-weighted mean redshift in each bin. The vertical error bars show the 68% confidence intervals. Note that these means lie above the median results for the individual systems both because we calculate the means from the linear metallicities (Equation 19) and because of the influence of high column density, high metallicity systems. The binning in redshift is arbitrary, though with an eye toward including at least ≈ 15 systems in each bin. The H I-weighted mean metallicity of neutral gas in the Universe increases slowly from high to low redshift, rising by an order of magnitude from $z \approx 5$ to 0.

3.5. Census of Metals in the Universe

Two decades ago, Pettini (1999) and other subsequent works noted the paucity of metals compared with expectations in the available data at $z \approx 2$. Their expectations were based on some of the earliest estimates of the star formation rate density evolution of the Universe,

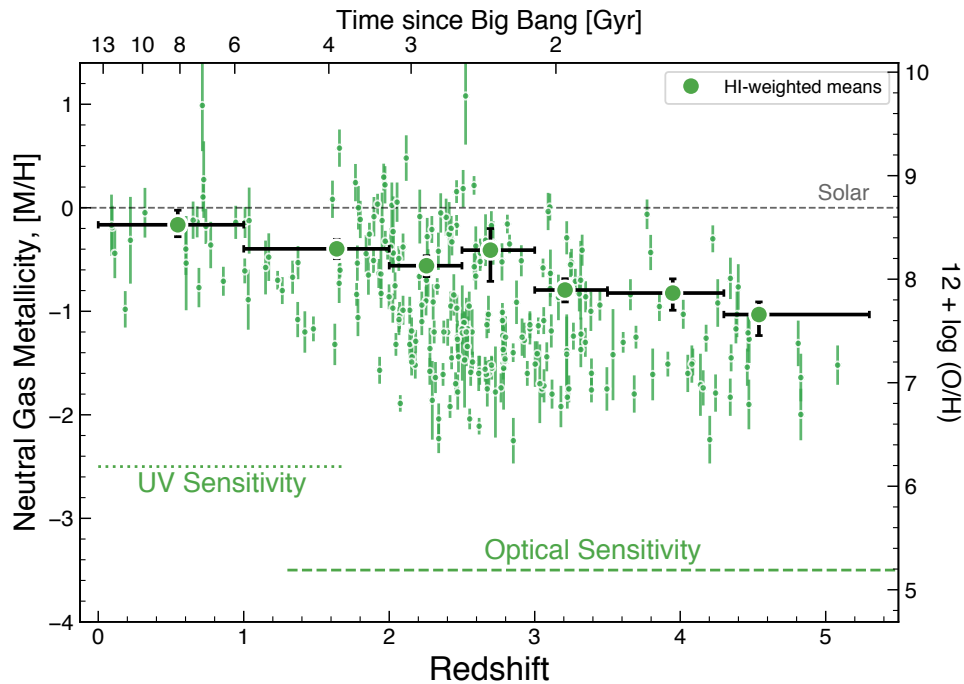


Figure 7

Metallicity measurements, expressed as $[M/H]$, for absorbers tracing neutral gas in the Universe ($\log N(\text{H I}) \geq 20.3$). The metallicities include corrections for dust depletion using the empirical approach of De Cia et al. (2018). The larger points with error bars are H I-weighted means with redshift. The increase in the weighted mean metallicity to lower redshift is modest, with a rise of ~ 1 dex from $z \approx 5$ until today. The scatter in the population at any redshift is larger than the overall increase in the mean. Lower metallicity gas than that seen in this statistical sample could readily be found: typical sensitivities (shown as dotted/dashed lines) are 1-2 orders of magnitude below the lowest observed metallicities.

Table 1 Mean metallicity and dust content of neutral gas absorbers

| $\langle z \rangle$ | z range | Num. ^a | $[\langle M/H \rangle]^b$ | $\log \langle \text{DTG} \rangle^c$ |
|---------------------|--------------|-------------------|---------------------------|-------------------------------------|
| 0.55 | [0.00, 1.00) | 18 | $-0.16^{+0.14}_{-0.11}$ | $-2.57^{+0.17}_{-0.16}$ |
| 1.64 | [1.00, 2.00) | 40 | $-0.40^{+0.09}_{-0.09}$ | $-2.87^{+0.11}_{-0.11}$ |
| 2.26 | [2.00, 2.50) | 62 | $-0.56^{+0.10}_{-0.11}$ | $-3.02^{+0.13}_{-0.15}$ |
| 2.70 | [2.50, 3.00) | 57 | $-0.41^{+0.21}_{-0.30}$ | $-2.75^{+0.25}_{-0.47}$ |
| 3.21 | [3.00, 3.50) | 38 | $-0.79^{+0.11}_{-0.12}$ | $-3.32^{+0.15}_{-0.16}$ |
| 3.95 | [3.50, 4.30) | 21 | $-0.82^{+0.14}_{-0.17}$ | $-3.43^{+0.17}_{-0.22}$ |
| 4.54 | [4.30, 5.30) | 14 | $-1.03^{+0.12}_{-0.20}$ | $-3.62^{+0.14}_{-0.26}$ |

^aNumber of absorbers in each redshift bin; ^bH I-weighted mean metallicity (§3.4; Figure 7); ^cH I-weighted mean dust-to-gas mass ratios, DTG (§4.1; Figure 11).

measurements of metals in neutral gas, and stellar metals from high-redshift galaxies. This *missing metals problem* spurred many follow-up works and thinking about the global distribution of metals in the Universe. Today we have significantly more complete information over a broad range of lookback times, covering $\approx 90\%$ of the age of the Universe. These

Cosmic Evolution of Neutral Gas Metallicity

The large samples of high-resolution absorption line measurements collected over the last two decades, coupled with empirical methods to account for the effects of dust grain depletion, provide robust measures of the metallicity up to $z \approx 5$. We show there is a mild metallicity evolution with cosmic time, but the scatter of the individual measures at a given redshift is larger than the total evolution. The lower bounds of the metallicity distribution are orders of magnitude larger than observational sensitivities at all redshifts: pristine material is exceedingly rare in neutral gas.

include greatly increased information on the evolution of the star formation rate density (as summarized in Madau & Dickinson 2014), as well as large samples of quasar absorbers with robust metallicity measurements that include a consistent treatment of the dust depletion, as summarized in §3.4. These facts motivate a reassessment of the cosmic evolution of the classical missing metals problem.

3.5.1. Total Metal Mass Density Produced by Stars. To compare to the measured metal densities and their evolution, we estimate the total amount of metals produced by star formation as a function of redshift which is developed in the rest of §3. We scale the stellar mass density in long-lived stars and stellar remnants by an estimated yield following Madau & Dickinson (2014). We write the total comoving metal mass density produced by stars as

$$\rho_{\text{metals}}(z) = y\rho_{\star}(z), \quad 20.$$

where y is the integrated yield of the stellar population. In this case the stellar mass density is that remaining in long-lived stars, derived by integrating the star formation rate density, $\psi(z)$, over time / redshift:

$$\rho_{\star}(z) = (1 - R) \int_0^{t(z)} \psi(z) \left| \frac{dz}{dt} \right| dt. \quad 21.$$

In this context R is the return fraction, the fraction of the stellar mass that is immediately returned to the gas when massive stars explode. Here we adopt results for a Chabrier (2003) initial mass function (IMF), which gives $R = 0.41$ if we assume instantaneous recycling for stars more massive than $m_0 \approx 1 \text{ M}_{\odot}$ (Madau & Dickinson 2014). We note that the choice of IMF is not affecting the results as the metal production rate is directly related to the mean luminosity density.

We adopt a simplified yield $y = 0.033 \pm 0.010$, drawn from the discussion in Peebles et al. (2014) with an error which encompasses the uncertainties associated with model assumptions and differing nucleosynthetic inputs. The Chabrier IMF gives results consistent with direct observations of stellar mass density at $z \approx 0$ compiled by Madau & Dickinson (2014), though, e.g., $\approx 0.1 - 0.2$ dex higher than the recent results of Driver et al. (2018). Adopting a total metal yield ignores complexities of the stellar sites of metal production (esp., the time lag associated with metals produced by type Ia supernovae and AGB stars) and the potential for metallicity-dependent yields. However, we are most interested in the global metal content of the Universe for times at which several non-primordial populations have contributed metals, and this yield provides an estimate the *total* metal output.

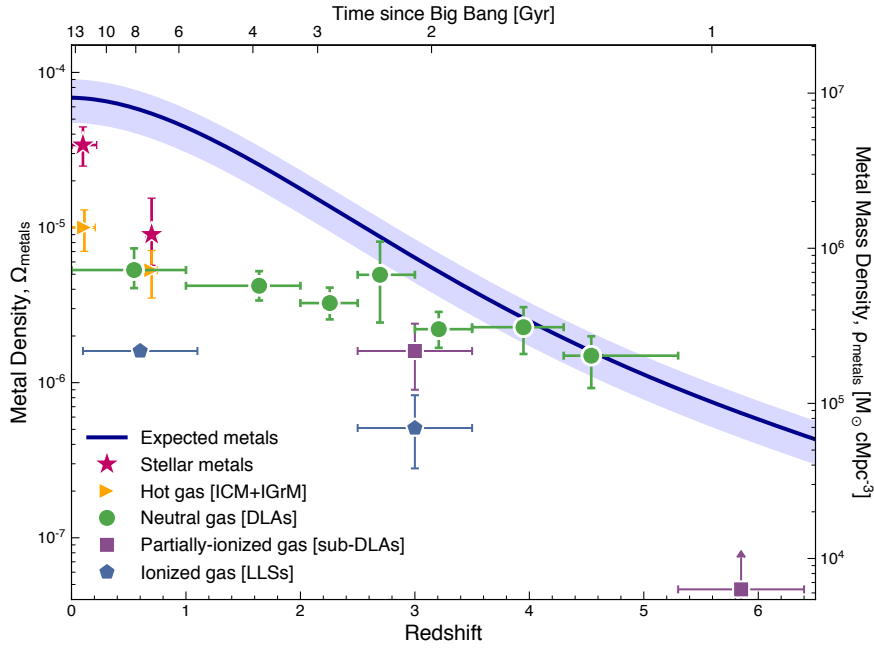


Figure 8

Global census of the metals in the Universe traced by the evolution of the cosmic metal densities compared with the expected amount of total metals ever output. The data points focus on robustly-observed contributors. For this reason the data are primarily representative of high density matter and have varying degrees of completeness with redshift. The lower limit at $z \sim 6$ is from the O I measurements of Becker et al. (2011), which we treat as a lower limit to allow for the elements not cataloged. After the dust depletion correction is uniformly applied, we find that the metallicity in the neutral gas dominates the metallicity of ionised gas.

3.5.2. Metal Mass Densities Traced by Absorption. We combine absorption-line derived metal abundances of distant gas with the cosmological density of the same absorbers, Ω_{gas} , to assess the contribution of neutral and more ionised gas to the total metal content of the Universe. Critically, this approach to assessing metal abundances is applied uniformly with redshift, until $z \approx 5$. To calculate the cosmological density of metals associated with absorption line systems, we combine the H I-weighted mean metallicity of the absorbers with Ω_{gas} :

$$\Omega_{\text{metals}} = \Omega_{\text{gas}} \langle Z_{\text{gas}} \rangle, \quad 22.$$

where $\langle Z_{\text{gas}} \rangle$ is the mean metal abundance by mass in the absorbers. Although we calculate $\langle Z_{\text{gas}} \rangle$ explicitly, we find $\langle Z_{\text{gas}} \rangle \approx 10^{[(M/H)_{\text{gas}}]} Z_{\odot}$ (e.g., non-solar abundances have a small impact on the calculation; De Cia et al. 2016).

Figure 8 shows a non-exhaustive sample of the cataloged contributions to the cosmological metal density as a function of redshift. The metal density associated with neutral gas absorbers (the absorbers with $\log N(\text{H I}) \geq 20.3$) is shown with the same redshift bins as Figure 7. These values represent the total metals in these systems, i.e., including both

ICM: Intracluster
Medium
IGrM: Intragroup
Medium

the gas and dust (see also §4 below). These metal densities associated with neutral gas are summarized in Table 2. Contributions from lower column density absorbers are taken directly from their respective references, from Fumagalli et al. (2016) for the $z \approx 3$ results and Lehner et al. (2019) for $z \lesssim 1$. At the highest redshifts, probing the metals in absorption becomes difficult as the flux bluewards of the quasar Ly- α emission is suppressed by Ly- α forest absorption. Becker et al. (2011) measure the density of O I absorption at $z \approx 6$; we plot this point assuming $\Omega_{\text{metals}} \gtrsim \Omega_{\text{OI}}$ to allow for the elements not cataloged (O is $\approx 40\%$ of the solar metal mass). This point traces gas with $\log N(\text{H I}) \gtrsim 19.0$, and likely is dominated by the lower column density end of this range; thus we associate it with the partially-ionized absorber range.

At lower redshifts where stars and hot gas found in groups and clusters play an important role, we also include the density of metals captured in stars and in the hot gas associated with clusters and groups of galaxies. We derive the quantity of metals sequestered in stars using the stellar metallicities as a function of galaxy stellar mass measured by Gallazzi et al. (2008) and Gallazzi et al. (2014) at $z \sim 0$ and $z \approx 0.7$, respectively, using the galaxy stellar mass function from Wright et al. (2018) (errors from Monte Carlo sampling). We derive the combined intragroup medium (IGrM) and intracluster medium (ICM) metal densities using a mass integral of the product of the halo mass function (Bocquet et al. 2016, as implemented in the COLOSSUS code of Diemer 2018), the hot gas baryonic fraction with mass (Chiu et al. 2018), and a global metallicity $Z_{\text{IGrM}} \approx Z_{\text{ICM}} \approx \frac{1}{3}Z_{\odot}$, assumed to be constant with redshift and halo mass (Mantz et al. 2017; Yates et al. 2017). For both the stellar and hot gas (ICM+IGrM) cases we assume our adopted solar metal abundance.

Table 2 Cosmic mass densities in neutral absorbers

| $\langle z \rangle$ | z range | Num. ^a | $\log \Omega_{\text{neutral gas}}^b$ | $\log \Omega_{\text{metals}}^c$ | $\log \Omega_{\text{dust}}^d$ | $\log \Omega_{\text{metals}}^{\text{expected}}^e$ |
|---------------------|--------------|-------------------|--------------------------------------|---------------------------------|-------------------------------|---|
| 0.55 | [0.00, 1.00) | 18 | $-3.23^{+0.01}_{-0.01}$ | $-5.27^{+0.14}_{-0.12}$ | $-5.79^{+0.17}_{-0.16}$ | -4.24 ± 0.13 |
| 1.64 | [1.00, 2.00) | 40 | $-3.10^{+0.01}_{-0.01}$ | $-5.38^{+0.09}_{-0.09}$ | $-5.97^{+0.11}_{-0.11}$ | -4.59 ± 0.13 |
| 2.26 | [2.00, 2.50) | 62 | $-3.04^{+0.01}_{-0.01}$ | $-5.49^{+0.10}_{-0.11}$ | $-6.07^{+0.13}_{-0.15}$ | -4.86 ± 0.13 |
| 2.70 | [2.50, 3.00) | 57 | $-3.01^{+0.01}_{-0.01}$ | $-5.30^{+0.21}_{-0.31}$ | $-5.77^{+0.25}_{-0.47}$ | -5.06 ± 0.13 |
| 3.21 | [3.00, 3.50) | 38 | $-2.98^{+0.02}_{-0.02}$ | $-5.66^{+0.11}_{-0.12}$ | $-6.30^{+0.15}_{-0.15}$ | -5.29 ± 0.13 |
| 3.95 | [3.50, 4.30) | 21 | $-2.94^{+0.02}_{-0.02}$ | $-5.64^{+0.13}_{-0.17}$ | $-6.37^{+0.17}_{-0.23}$ | -5.58 ± 0.13 |
| 4.54 | [4.30, 5.30) | 14 | $-2.91^{+0.02}_{-0.02}$ | $-5.83^{+0.13}_{-0.21}$ | $-6.53^{+0.15}_{-0.27}$ | -5.79 ± 0.13 |

^aNumber of absorbers in each redshift bin; ^bCosmic gas mass density at $\langle z \rangle$ (§2.1.2; Figure 3); ^cCosmic metal mass density in neutral gas (§3.5.2; Figure 8); ^dCosmic dust mass density in neutral gas (§4.2; Figure 12); ^eTotal expected cosmic metal mass density (§3.5.1; Figure 8).

Figure 8 therefore provides a global census of metal content of the Universe over a large look-back time. It includes only values that are the most robustly and directly measured. Thus, there are some redshift ranges for which fewer contributions are included and some contributions are not represented at all. The expected metals follow the stellar density of the Universe, rising by ≈ 2 orders of magnitude between $z \approx 5$ and $z \approx 0$. Consistent with the greatly diminished star formation rate density at low redshift, the curve flattens significantly at $z < 1$. By contrast, we see the metal density associated with neutral gas shows a much shallower rise with time, increasing by only a factor of ≈ 8 since $z \approx 5$. Remarkably, the metals associated with neutral gas alone are consistent with all the expected metal density of the Universe at $z \gtrsim 2.5$ (Rafelski et al. 2014). We note in passing that this leaves little room for a large population of metal-rich absorbers missed due to dust (§3.2.3).

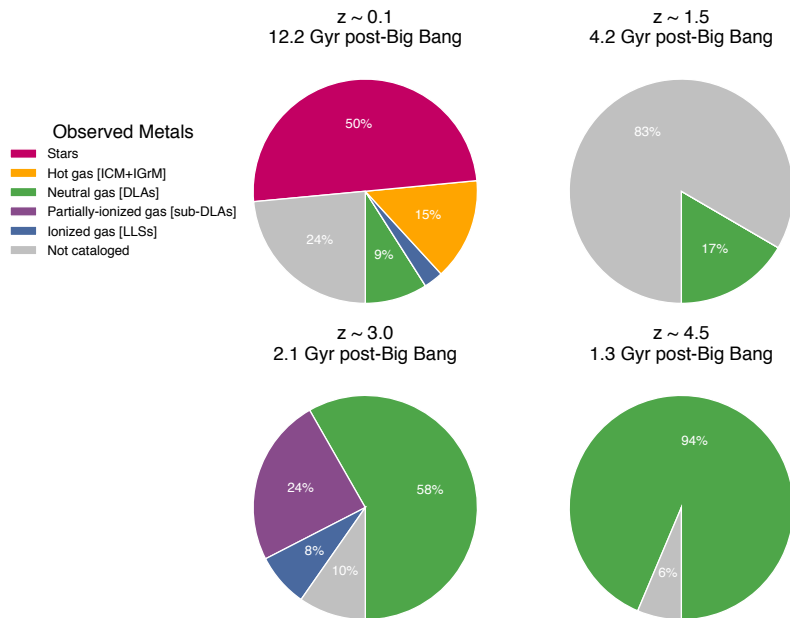


Figure 9

A modern census of metals showing the fractional contribution of directly-measured metal densities to the total expected based on the stellar densities at four redshifts. The estimate of the total metal mass densities assumes a yield $y = 0.033 \pm 0.010$; thus, when the proportion of the expected metals not cataloged in our census (grey) is $\lesssim 30\%$, the cataloged metals are consistent with expectations. At redshifts $z \gtrsim 2.5$, the vast majority of the expected metals are found in low-ionization gas in all its forms. At lower redshift, there is a greater diversity of contributors, though nearly all of the metals have been cataloged. At intermediate redshifts ($1 \lesssim z \lesssim 2$) the likely contributors are not yet robustly determined. Overall, the expected metal content of the Universe is largely accounted for.

This is further demonstrated in Figure 9, which shows the fractional contributions of the cataloged components to the expected metals at four distinct redshifts, $z = 0.1, 1.5, 3.0$, and 4.5 . At the higher redshifts, in the range $2.5 < z < 5$, essentially all of the expected metals are found in the cataloged classes of absorbers, including the partially-ionized ($19.0 \leq \log N(\text{H I}) \leq 20.3$) and ionized absorbers ($17.2 \leq \log N(\text{H I}) \leq 19.0$). Some previous reports found that the partially-ionized gas contributes more to Ω_{metals} than the neutral gas, whereas Figure 8 shows the opposite. The differences arise from different treatments of the inclusion of dust corrections in metallicity estimates. Overall, when dust corrections are applied to both column density ranges, all works agree the contribution of partially-ionized gas is less than the neutral gas (Péroux et al. 2007; Kulkarni et al. 2007, this work).

In general, the contributors to metals are more diverse at lower redshifts: stars, the hot gas (ICM+IGrM), and the ionised phase of the gas all become more important. The metals in the neutral phase contribute only a small fraction of the expected metals. Figure 9 shows that at $z \approx 0.1$, half of the metals are in stars and the metals in the hot gas (ICM+IGrM) become comparable to the metals in the neutral gas at $z \lesssim 1$.

3.5.3. Other Sinks of Metals. Figures 8 and 9 show that the metal densities cataloged here fall short of expectations at $z \lesssim 2.5$. We have focused on the components with the most robust measurements of their associated Ω_{metals} . However, there is existing guidance on components we have not included in our census. Working to progressively higher overdensities, the additional contributors include: the diffuse, photoionized intergalactic medium (the Ly- α forest, McQuinn 2016) and the low density and hot circumgalactic matter (CGM, Tumlinson et al. 2017). We note that the warm-hot intergalactic medium (WHIM) in simulations was originally identified as a large baryon reservoir, including 30-50% of the baryons at low redshift (Cen & Ostriker 1999; Davé et al. 2001). In today’s view, most of the metals originally connected to the WHIM are identified with the CGM (Werk et al. 2014).

At the lowest density scale, the Ly- α forest traces diffuse intergalactic gas in the dark matter filaments threading the Universe (at H I column densities well below $\log N(\text{H I}) \leq 17.2$). At high-redshift, the Ly- α forest houses the majority of the baryons in the Universe and is photoionized material (with $T \sim 10^4$ K). However, the metal content of this matter is low. For example, the results of D’Odorico et al. (2013) imply $\Omega_{\text{metals}}^{\text{Ly}\alpha} \approx 1.4 \times 10^{-7}$ at $z \approx 3$ (where we have corrected their estimate from carbon to the total metal content). This contribution is unimportant compared with the neutral gas at these redshifts. At low-redshift, diffuse large-scale structures house both photoionized and collisionally-ionized baryons. The metal density of these constituents is assessed through censuses of metal lines associated with low column density H I absorbers. At $z \lesssim 1.5$, Shull et al. (2014) argue for $\Omega_{\text{metals}}^{\text{Ly}\alpha} = (1.1 \pm 0.6) \times 10^{-5}$.

The denser gas on the scale of galaxy halos also contains highly-ionized material that houses significant quantities of metals (Tumlinson et al. 2017). This gas, traced by Si IV, C IV, N V, and O VI, likely arises through photoionization of low density gas as well as in interfaces of isolated cold gas (clouds) with a hotter medium, in shocks propagating through these clouds, or in diffuse $T \gtrsim 10^5$ K gas (e.g., Lehner et al. 2014; Stern et al. 2016). The uncertainties in the ionization mechanisms and ion fractions limit the precision with which the total metal budget of this material is estimated. For predominantly neutral gas ($\log N(\text{H I}) \gtrsim 20.3$), the contribution of associated high ionization species to their metal budget is of order 10% (Lehner et al. 2014). The fraction of metals associated with these high-ionization species increases at lower H I column densities. For the partially-ionized and ionized gas, these metals likely become dominant. At $z \approx 2.5$ –3.5, Lehner et al. (2014) estimated $\Omega_{\text{metals}} \approx (1.5 - 6) \times 10^{-6}$.

3.5.4. Is There a Missing Metals Problem? The “missing” metals problem poses the question: which baryonic components of the Universe host the metals? In the results summarized in Figures 8 and 9, we are observing the greatest sinks of metals change. At high redshift, $z \gtrsim 2.5$, the neutral gas houses nearly all of the available metals, while at low redshift, $z < 1$, the metals are distributed nearly equally between stars and a broad range of gaseous environments. This reflects the build up in the typical mass scale of halos toward low redshift and the influence of energetic feedback over time.

These results are distinguished from historical measures (e.g., Pettini 1999; Pagel 1999; Ferrara et al. 2005) in several ways. First, the results presented here span the full range of redshifts $0 < z \lesssim 5$, covering $\approx 90\%$ of the age of the Universe. At higher redshifts ($z \gtrsim 2.5$), the metals associated with high column density absorbers are readily able to match the expected quantity of metals made by stars. The historical results were constrained to a redshift range at which the expected metals start to diverge significantly

Update on the Missing Metals Problem

We have compiled a census of metals in the Universe and compared this to a new assessment of the total metal production by star formation (Madau & Dickinson 2014). At high redshift, $z \gtrsim 2.5$, neutral gas in the Universe contains most of the expected metals. At low redshift, $z \lesssim 1$, the set of contributors is more diverse, and stars are the dominant contributor. At intermediate redshifts, the likely contributors are yet to be fully characterized; upcoming efforts will account for some of these (e.g., stars), while a complete census will require new facilities, notably in the UV and X-ray. Overall, the expected metal content of the Universe is likely accounted for, in contrast to the missing metals problem identified 20 years ago (Pettini 1999; Pagel 1999).

from the metal densities in neutral gas ($z \approx 2$; Pettini 1999; Ferrara et al. 2005; Bouché et al. 2007). At low redshift ($z \lesssim 1$), it is likely that metals found in stars, the hot gas in groups and clusters, highly-ionized CGM gas, and the Ly- α forest each contribute metals in quantities similar to that seen in the neutral gas, which is sufficient to then close the budget over this redshift regime.

There are clearly redshift ranges for which a full, robust accounting is not available (e.g., the $z \sim 1.5$ panel of Figure 9) due to the difficulty in observing the relevant metals in this regime. Using the lower redshifts as a guide, we expect the metal budget to be closed through deeper NIR spectral surveys of stellar metals, deep X-ray observations of hot gas in the IGM+IGrM, and deep UV surveys of CGM and Ly- α forest metals to higher redshift. Probing the gas to higher redshifts will require new facilities. The next generation of X-ray facilities (*Athena*, *Lynx*) will provide robust measurements of Ω_{metals} in the ICM up to $z \approx 2$ (Cucchetti et al. 2018) and allow some absorption line measurements of the ionized phase. Proposed UV facilities (*LUVOIR*, *HabEx*) will allow constraints on IGM and CGM metals to intermediate redshifts. Between the contributions summarized in Figures 8 and 9 and the additional tracers of lower-density and/or hotter matter in §3.5.3, the expected metal content of the Universe is largely accounted for.

4. COSMIC EVOLUTION OF DUST

A substantial fraction of all the metals produced in the Universe are locked into solid-phase dust grains. Such dust not only has a strong influence on the observational properties of galaxies, but it is critical in the thermal balance of gas as well as in shielding the cores of dense clouds from UV radiation, allowing the formation of molecules critical to the star formation process. Hence the cosmic evolution of dust mass is a fundamental measure of galaxy evolution. There are still significant unknowns in the manner in which dust is created and ultimately destroyed. Thus significant effort has been put into understanding the galactic scaling relationships that apply to dust, including the relationship between local metallicity and dust content – traced through the dust-to-gas ratio (DTG) or dust-to-metals ratio (DTM), as well as the global dust content of the Universe traced through the dust density, Ω_{dust} . In this section, we use the corrections for dust depletion from §3 to estimate the dust properties of neutral absorbers and estimate the dust density evolution of the Universe.

DTG:
dust-to-gas ratio

DTM:
dust-to-metals ratio

4.1. Basic Principles of Assessing the Dust in the Universe

The characterization of the bulk statistical properties of dust involve assessing the DTG or DTM. The former is the fraction of the interstellar mass locked into dust grains; the latter is the fraction of the metal mass incorporated into the solid phase. In the Milky Way, the global values of these quantities – based on modeling the infrared emission and optical/UV extinction – are $\text{DTG} \approx 0.006$ and $\text{DTM} = \text{DTG} Z_{\odot}^{-1} \approx 0.45$ (e.g., Draine & Li 2007). Significant work has been put into characterizing these quantities in galaxies beyond the Milky Way, assessing observational constraints both on the integrated values (e.g., Rémy-Ruyer et al. 2014; De Vis et al. 2019) and spatially-resolved values within galaxies (e.g., Vílchez et al. 2019). These works have placed particular emphasis on the variation in DTG and DTM ratios with metallicity, stellar mass, star formation rate, and gas content of the galactic environments, as these help shape our understanding of the factors that drive the formation/destruction balance of dust.

The dust depletion corrections used to assess the total metal content of neutral absorbers in §3 have an important by-product: the derived corrections are measures of the metal content of dust grains in the environments traced by the absorption lines. Parallel to our derivation of Ω_{metals} , we use these results to assess the cosmological dust density of the Universe:

$$\Omega_{\text{dust}} \equiv \rho_{\text{dust}}/\rho_{\text{crit},0} = \langle \text{DTG} \rangle \Omega_{\text{gas}}, \quad 23.$$

where $\langle \text{DTG} \rangle$ is the mean dust-to-gas mass ratio. The DTG ratios for individual absorption systems are derived from elemental depletions; because the behavior of each metal species varies (Jenkins 2009; Jenkins & Wallerstein 2017), we build up the total DTG on an element-by-element basis. This starts from an estimate of the depletion, δ_X , for each individual element, X , derived from the dust sequences of De Cia et al. (2018). The (logarithmic) depletion is defined:

$$\delta_X = \log N(X)/N(\text{H}) - \log Z_{\text{abs}}^X/Z_{\odot}^X, \quad 24.$$

where Z_{abs}^X is the abundance by mass of X in the absorber and Z_{\odot}^X the equivalent in the Sun. The dust-to-metal ratio for an individual element, X , is related to its depletion:

$$\text{DTM}_X = 1 - 10^{\delta_X} \quad 25.$$

(e.g., Vladilo 2004; De Cia et al. 2016). The dust-to-gas mass ratio for an individual element can then be written as

$$\text{DTG}_X = \text{DTM}_X Z_{\text{abs}}^X, \quad 26.$$

which is related to the measured $[\text{M}/\text{H}]$ through

$$\text{DTG}_X = (1 - 10^{\delta_X}) Z_{\text{abs}}^X = (1 - 10^{\delta_X}) (10^{[\text{M}/\text{H}]} 10^{[X/\text{M}]} Z_{\odot}^X). \quad 27.$$

Here we use the intrinsic metallicity of the absorber, $[\text{M}/\text{H}]$, and allow for non-solar relative abundances $[X/\text{M}]$. Ultimately this provides the mass of an element X incorporated in dust relative to the total gas mass in the absorber. The total DTG is the sum over all elements, $\text{DTG}_{\text{abs}} = \Sigma \text{DTG}_X$.

Practically speaking, it is sufficient to consider only $X = \{\text{C}, \text{O}, \text{Si}, \text{Mg}, \text{Fe}\}$ in the sum, as together these represent the vast majority of the dust mass (see Draine 2011). The depletions of each of these five elements are coupled through the dust sequences derived by De Cia et al. (2018). Observations of relative metal abundances constrain the overall

level of depletion, characterized using δ_{Fe} as reference. The observed metals then predict the depletions of all of the metals. We assume a solar mixture of elements for all but Fe, which shows an empirical under-abundance compared with the α elements (De Cia et al. 2016), and $[\text{C}/\text{Fe}] \approx 0$, allowing for an under-abundance of C in lower-metallicity systems (e.g., Jenkins & Wallerstein 2017).

Carbon makes up $\sim 30\%$ of the dust mass in the Milky Way (Draine 2011), but there are not good measurements of C/H in quasar absorbers from which to build up a depletion sequence, as lines from the dominant ionization states of C are typically saturated or too weak to observe. Observations of C absorption in the Milky Way are also limited, for the same reasons. Even though these have significant uncertainties, we adopt the relationship between δ_{Fe} and δ_{C} from Jenkins (2009).

The characteristics of the DTG and DTM ratios as a function of absorber metallicity are summarized in Figure 10 and are listed in Supplemental Table 1. The upper panel shows the DTG ratio with metallicity. The dotted line is the maximum allowed DTG ratio, where all the metals are incorporated into grains. The position of the Milky Way is shown by the large cross. Also shown are best-fit trends in DTG ratios for local galaxies derived from far-infrared observations by Rémy-Ruyer et al. (2014) and De Vis et al. (2019); while there are many such results, these are typical of the range of results seen at low redshift. The bottom panel shows the DTM ratio as a function of metallicity. Where carbon is the only significant contributor to the dust content, we treat these values as upper limits.

The DTG ratio is a strong function of metallicity, as expected. It is noteworthy that the neutral gas follows the trends seen in low-redshift galaxies at high metallicities ($[\text{M}/\text{H}] \gtrsim -1$); there is little evidence that the DTG behaves differently with redshift. The neutral gas measurements extend to a metallicity regime lower than found in low-redshift galaxies. A portion of the population shows DTG ratios that extend the trend seen at higher metallicity, while a significant fraction falls well below this trend due to lower DTM ratios. This suggests a change in the dust assembly at low metallicities.

We plot the DTG measurements for individual absorbers in Figure 11 as function of redshift, in parallel to Figure 7 summarizing the metallicity evolution of these systems. The H I-weighted mean values are shown as larger points with error bars. The characteristic DTG for the Milky Way is also shown, $\text{DTG}_{\text{MW}} \approx 0.45 Z_{\odot}$ (Draine & Li 2007, renormalized following recommendations in Draine et al. 2014). The mean DTG ratio increases by ~ 1 dex from $z \approx 5$ until today, a result of the increase in mean metallicity.

4.2. Cosmological Dust Mass Densities

The global evolution of the dust mass in the Universe is captured by the dust density, Ω_{dust} . By analogy to the metal densities, this is the comoving density of dust in the Universe normalized by the critical density, $\Omega_{\text{dust}} \equiv \rho_{\text{dust}}/\rho_{\text{crit},0}$. We derive values of Ω_{dust} in the neutral gas of the Universe following Equation 23. We adopt H I-weighted mean DTG ratios, which we write in parallel to the mean metallicity of Equation 22:

$$\langle \text{DTG} \rangle = \frac{\Sigma(\text{DTG} \times N(\text{H I}))}{\Sigma N(\text{H I})} \quad 28.$$

Figure 12 shows the values of Ω_{dust} in neutral gas derived in this way from $z \approx 5$ to today. Systems possibly missed due to the dust sample bias caveat mentioned in §3.2.3 are not accounted for. The evolution of Ω_{dust} follows a similar trend as that for Ω_{metals} in neutral gas, increasing by a factor of ≈ 7 between the $z \approx 5$ and today. That the dust tracks

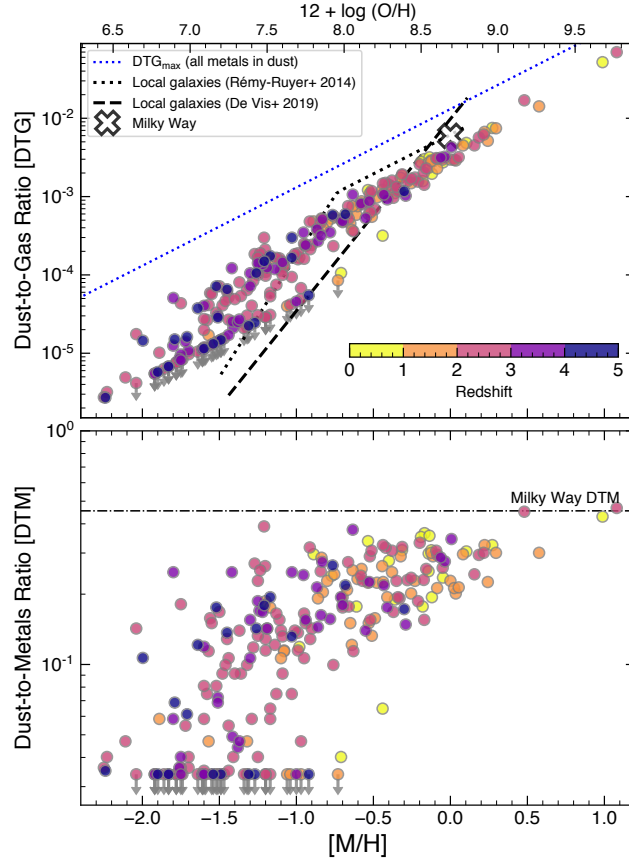


Figure 10

Properties of dust in neutral gas as a function of absorber metallicity. *Upper:* The dust-to-gas mass ratios, DTG, color coded by redshift. The dotted line is the limit in which all metals are incorporated into grains (DTM = 1). The position of the Milky Way is shown. The black lines show fits to the properties of local galaxies derived from far-infrared emission (Rémy-Ruyer et al. 2014; De Vis et al. 2019). The DTG values derived for neutral gas over all redshifts follow trends seen in these low-redshift galaxies, extending these measurements to a lower metallicity regime. *Lower:* The dust-to-metal mass ratio, DTM, giving the fraction of all of the metal mass bound into dust. The dot-dashed line represents the DTM ratio in the Milky Way (Draine & Li 2007; Draine et al. 2014). Upper limits are due to the uncertainty in carbon depletion. With decreasing metallicity, the DTM values both decrease and show increased scatter, reflecting complex dust chemistry at work in these low-metallicity environments.

the evolution of the metal density is not surprising, as the dust mass in any individual system is related to its metallicity (e.g., Figure 10). The overall shape resembles estimates of $\Omega_{\text{molecular gas}}$ (Figure 4).

Figure 12 also shows Ω_{dust} derived through other means, of which there are three main approaches. The first approach integrates dust mass functions derived from modeling the spectral energy distributions (SEDs) of individual galaxies as a function of redshift. Selected

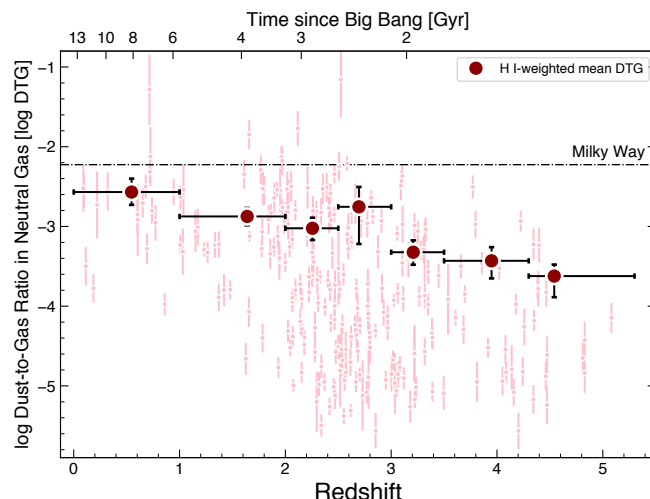


Figure 11

The dust-to-gas mass ratio, DTG, in neutral gas absorbers as a function of redshift. The mean values weighted by H I column are shown as large points with error bars. The Milky Way value from Draine & Li (2007) renormalized following Draine et al. (2014) is shown. The evolution in redshift mirrors that of the metals that provide the source material for grains (see Figure 7), with the mean DTG increasing by ~ 1 dex from $z \approx 5$ to $z=0$. The DTG values show an even larger spread at a given redshift than the metallicities. This reflects the large scatter in the DTM at low metallicities and the broad range of metallicities probed by these absorption line measurements.

results derived in this way are shown in Figure 12 (Dunne et al. 2011; Beeston et al. 2018; Driver et al. 2018; Pozzi et al. 2019). They rely on the inclusion of mid- or far-infrared measurements from, e.g., *Spitzer*, *WISE*, and *Herschel*, as well as detailed models to assess the total dust mass of galaxies. The results from the three studies in Figure 12 are in respectable agreement over their common redshift range. The second approach derives and integrates over a luminosity function of galaxies from the power spectrum of the far-infrared background radiation (De Bernardis & Cooray 2012; Thacker et al. 2013). Results derived from *Herschel* observations of the background are shown as a shaded region in Figure 12. The third approach assesses the density of dust based on its reddening or extinction of background optical sources (triangles in Figure 12). Ménard et al. (2010) derived the dust profiles about $z \sim 0.3$ galaxies, while Ménard & Fukugita (2012) derived Ω_{dust} using the extinction due to Mg II absorbers. A fraction of the Mg II absorbers selected by Ménard & Fukugita (2012), with equivalent widths $\text{EW} > 0.8 \text{ \AA}$, trace the neutral gas studied here ($\log N(\text{H I}) \geq 20.3$; Rao et al. 2017). The remainder is associated with lower-density circumgalactic gas. We see good agreement over the redshift range of overlap in the values of Ω_{dust} derived for neutral gas with those derived through other means. However, the depletion-based results reported here trace Ω_{dust} to significantly higher redshifts than the other methods, providing a measure of the build-up of dust from $z \approx 5$. The depletion-based results for neutral gas are based on counting atoms incorporated into grains and make no assumptions on the physical properties (such as opacity or temperature) of the dust.

Taking the whole of the observations, Ω_{dust} peak around $z \sim 1$ (~ 8 Gyr ago), suggesting

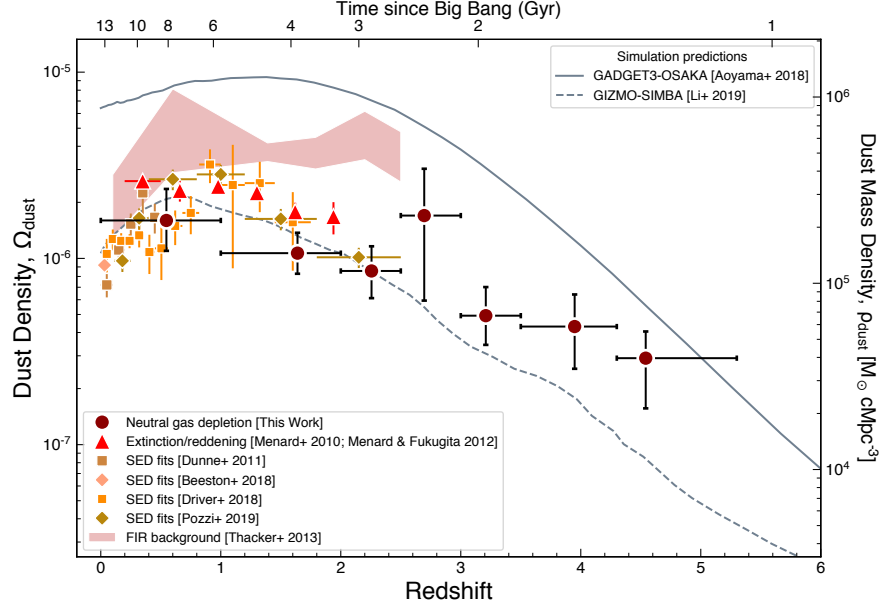


Figure 12

Evolution in cosmological dust density, Ω_{dust} , derived through different approaches. Our assessment of the cosmological dust mass density for neutral gas is shown with large points with error bars. We show several measures of Ω_{dust} derived from large samples of individual galaxies; their dust content is assessed using attenuations derived from optical SED fits or from SED fits to optical through FIR emission. Estimates of the dust mass density from the power spectrum of the far-infrared background are shown as the shaded band. Dust in and around galaxies (esp. in the CGM) is probed through the reddening or extinction associated with Mg II systems or foreground galaxies. Recent predictions from cosmological hydrodynamic simulations incorporating on-the-fly dust tracking are also shown by lines. The cosmological dust mass density associated with neutral gas (which is inclusive of neutral gas in the ISM and CGM of galaxies) increases by nearly a dex from $z \approx 5$ to $z \approx 1$, following a trend similar to that for Ω_{metals} in neutral gas. At $z < 2$, the measurements from disparate techniques show good agreement. Measurements of dust in neutral gas give a uniform observational constraint on the global build-up of dust from $z \approx 5$ to today.

that dust formation is either concurrent with star formation or lags no more than a few Gyr behind the star formation peak (Madau & Dickinson 2014). There is a smooth decline in the values of Ω_{dust} over the past 8 Gyr, implying that the Universe is becoming more transparent. The physical cause of this turn-down is not well understood; hypotheses include the net destruction of grains or their ejection from galaxies (e.g., Popping et al. 2017; Li et al. 2019). Several recent works have predicted the global evolution of dust in semi-analytical models (e.g., Popping et al. 2017; Millán-Irigoyen et al. 2019; Vijayan et al. 2019; Graziani et al. 2019) and by incorporating self-consistent dust physics on-the-fly into bona fide hydrodynamic simulations (e.g., Bekki 2015; Aoyama et al. 2018; McKinnon et al. 2018; Hou et al. 2019; Li et al. 2019). These latter works account at the sub-grid level for the processes of grain production (e.g., stellar or supernova production, ISM accretion) and destruction (e.g., by shattering / sputtering in hot gas / shocks, X-ray heating driven by

AGN, astration). We show the results for dust in galaxies from two simulations in Figure 12 (Aoyama et al. 2018; Li et al. 2019). Their outcomes in Figure 12 show similar slopes characterizing the dust mass build-up to $z \gtrsim 2$. However, due to differing assumptions about grain production and destruction at the sub-grid level, there is significant variation between them in both the total dust density predicted and the low redshift behavior. The variations in these results are indicative of the uncertainties remaining in dust modeling in a cosmological context. The emerging field of dust measurements at high redshift will provide additional constraints on the sub-grid physics important for such modeling.

Cosmic Evolution of Dust

We have used the multi-element methods for correcting elemental depletion to estimate the amount of the metals locked into dust grains in neutral gas. We derive the dust-to-gas ratio (DTG) in neutral absorbers, extending such measurements to lower metallicities than are available in the local Universe. We find the H I-weighted DTG increases by ~ 1 dex from $z \approx 5$ to today, in parallel to the increase in mean metallicity. We combine these DTG estimates to derive the global dust density of the neutral gas over $0 \lesssim z \lesssim 5$, showing a gradual increase in the amount of dust in the Universe over time. Our findings are broadly in agreement with measurements of the dust density found in galaxies at $z \lesssim 2$. These measurements will provide new constraints to the next generations of hydrodynamical simulations incorporating dust physics to understand the galaxy contributors to the global build-up of dust.

5. LOOKING FORWARD AND CONCLUSIONS

In this review, we have described observational constraints on the global evolution of gas, metals, and dust over cosmic time. The progress in the field in the last two decades, both observationally and in terms of simulations, has been truly remarkable.

5.1. Pushing from the global to the local

The topics covered in this review refer to global quantities averaged over the contributions from many environments. The strength (and the limitation) of such density estimates is that they are made regardless of the precise nature of the absorbers. However, the ultimate goal is to characterize the connection between the components depicted in Figure 1 and these global properties. Important progress in this field will require breaking down the types and properties of the environments that contribute to the metal mass densities in Figure 8 as a function of redshift.

Absorbers tracing neutral gas (with $\log N(\text{H I}) > 20.3$) are strongly associated with galaxies. We have witnessed an explosion of the number of galaxies found to be associated with such absorbers. While early efforts had low success rates, the turning point in identifying and connecting galaxies to such absorbers has been the use of 3D-spectroscopy at near-infrared (*VLT/SINFONI*, *Keck/OSIRIS*), optical (*VLT/MUSE*, *Keck/KCWI*) and millimeter (*ALMA*) wavelengths (e.g., Bouché et al. 2016; Péroux et al. 2017; Hamanowicz et al. 2020). Among the most surprising aspects of such work has been the detection of strong CO emission from galaxies associated with quasar absorbers, implying large molecular masses (Neeleman et al. 2016; Klitsch et al. 2018).

These galaxy identifications draw a picture in which the gas selected in absorption is often not uniquely associated with a single luminous galaxy. Understanding the environments that contribute to the global baryonic, metal, and dust censuses described in this review will require the compilation of large samples of such identifications in order to dissect the contributors (Péroux et al. 2019). Currently, best efforts combine the dynamics, kinematics and metallicity information to relate the neutral, ionised and molecular phase of the gas component by component (Bouché et al. 2012; Rahmani et al. 2018).

Results from simulations predicting poor metal mixing have motivated observers to use close quasar pairs (Rubin et al. 2018) as well as multiple images from gravitationally lensed background objects to probe the transverse small-scale coherence along sightlines dozens of kpc apart (Chen et al. 2014; Rubin et al. 2018). Using extended objects as background source provide continuous map of absorbers on small scales (Cooke & O’Meara 2015; Lopez et al. 2018; Péroux et al. 2018). The spatial resolution of the instrument is a key factor for these works. In the future, an increased number of targets will be within reach thanks to the collecting area of the next generation of telescopes combined with IFU capabilities such as the *ELT/HARMONI* instrument. At higher redshifts, bright targets will be within reach of *JWST*. At lower redshifts, *BlueMUSE/VLT* will provide bluer coverage with a large field-of-view thus increasing the number of accessible targets for such detections (e.g. *Messier*).

Eventually, a more direct probe of the extent of gas and metals around galaxies will come from their direct detection in emission. Circumgalactic gas has been detected through stacking of narrow-band images of galaxies which revealed diffuse Ly- α haloes extending up to several dozens of kpc (Steidel et al. 2011; Momose et al. 2016). More recently, *VLT/MUSE* observations have revealed Ly- α haloes around individual emitters (Leclercq et al. 2017; Wisotzki et al. 2018). The construction of the *Dragonfly* experiment, able to probe low surface brightnesses, from commercially-available cameras (Abraham & van Dokkum 2014) demonstrates that new observational parameter space can be explored without necessarily relying on novel technological development. Emission experiments, however, constitute a considerable challenge at higher redshifts given the cosmological surface brightness dimming scales as $(1+z)^{-4}$. Dedicated UV-facilities may play a critical role in the characterization of metals and gas around galaxies. An example is *FIREBall*, a balloon-borne 1-m telescope coupled to an ultraviolet spectrograph (Hamden et al. 2019), though larger missions have been proposed.

Large-scale models of the Λ CDM Universe predict a structure made of sheets and filaments of dark matter arranged in a *cosmic web*. The gas that we have characterized in this review – largely found within galaxy halos – is affected by the environment of those halos (Kraljic et al. 2019). The ionized gas needed to resupply the neutral and molecular gas consumed by star formation (Figure 5) is ultimately drawn from the filaments within which galaxies are embedded. We can characterize the connection of this large scale structure to halos with 3D tomographic maps using absorption lines toward a sufficiently dense collection of background sources (Pichon et al. 2001; Lee & White 2016). A new generation of spectroscopic surveys will offer the prospect to reconstruct robustly the 3D structure of the cosmic web. In particular, Subaru *PFS* will map the three-dimensional gas distribution over a large cosmological volume at $2 < z < 3$ through a large spectroscopic survey. Later, the *MOSAIC* instrument will benefit from the collecting area of the *ELT* to further expand such studies.

5.2. Simulating Baryonic Processes in Cosmological Context

From a theoretical viewpoint, the level of complexity arises from the different scales involved: from large scale cosmological environment to pc scale interstellar physics which is both physically challenging to model and time-consuming to simulate. Over the past decade, advances in numerical methodologies and computing speed have allowed extraordinary progress in our ability to simulate the formation of structures. It is a remarkable achievement that the overall physical properties (density and temperature) of the gas (specially H I) in these models reproduce to observations of the absorbers column densities and line widths (Fumagalli et al. 2011; Rahmati & Schaye 2014, but see Gaikwad et al. 2017). However, even with today's most powerful computers, we are still far from being able to self-consistently simulate the formation of molecular clouds in a cosmological context. Simulating the multiphase interstellar medium (ISM) still remain challenging even in “zoom-in” simulations, so that it is necessary to make use of subgrid modules to model unresolved physical processes, such as the formation of molecular clouds, winds from dying stars, and supernovae (Teyssier & Commerçon 2019). Progress in understanding the global baryon cycle will have impact beyond understanding the evolution of star formation and galaxies. Indeed, the nature of this baryonic physics impacts the matter power spectrum and thus the inference of cosmological parameters from weak lensing measurements from next generation of surveys such as LSST, Euclid and WFIRST (Semboloni et al. 2011; Chisari et al. 2018; Foreman et al. 2019).

By including more realistic physics, simulations will be an essential tool to interpret current observations. One of the most pressing set of questions is to understand which objects and media contribute to the global quantities presented in this review. The main contributors to $\Omega_{\text{neutral gas}}$ have column densities centered around $\log N(\text{H I})=21.0$ (Péroux et al. 2003; Noterdaeme et al. 2012). The question remains as to which extent these are associated with the ISM of galaxies or with cold clumps in the CGM as well as how these contributions change with redshift. In addition, a better understanding of the cycling of baryons between H I and the ionized phase of the gas will likely come from improved simulations.

The inclusion of a full treatment of CO and H₂ will be crucial to interpret the flow of information on the molecular gas in the Universe afforded by ALMA and other mm facilities. Today, observations rely on a number of assumptions (Spectral Line Energy Distribution - SLED and CO-to-H₂ conversion factor) to relate CO to molecular hydrogen. A better understanding of how well does CO traces H₂ (as a function of temperature, density, metallicity and redshift) is imperative to make progress in this field. The most essential ingredients to be considered are non-equilibrium chemistry and cooling, both for molecular hydrogen and heavy elements, and particularly radiative transfer of ionizing and dissociating radiation (Richings et al. 2014; Pallottini et al. 2019). Together, these points will provide a better understanding of the contributors to the global evolution of molecular gas in the Universe, $\Omega_{\text{molecular gas}}$.

The metallicity and total metal content of the highly-ionised phase of the gas continue to constitute an important observational challenge. Observers rely on tracers such as CIV, SiIV or OVI, but relating these measures to the total amount of carbon or silicon depends strongly on ionization models (and poorly-constrained assumptions about the ionization mechanism). In addition, the mixing of metal clouds could remain incomplete (e.g. Schaye et al. 2007). Recently, several simulations (Churchill et al. 2015; Peeples et al. 2019) find that in the CGM, high ionization gas seen in absorption arises in multiple, extended structures

spread over ~ 100 kpc. Due to complex velocity fields, highly separated structures give rise to absorption at similar velocities (see also Bird et al. 2015). These authors predict a mismatch between the smoothing scales of H I and high-ionisation metals. Therefore depicting a realistic distribution of metals on galaxy scale will be of paramount importance to fully understand of the cycle of baryons.

Finally, a more complete treatment of dust production and destruction, a key catalyst for star formation, is also crucial (McKinnon et al. 2018; Li et al. 2019). On global scales, it will be a salient finding to explain the observed turndown of Ω_{dust} at low redshift. The distribution of dust about galaxies and the fraction of material expelled from bound systems will provide crucial information on our understanding of these quantities. The grain sizes and ultimately the composition of dust will further constrain the possible extinction and depletion central to the observational quantities derived in this review.

5.3. Concluding Remarks

Probing the Universe’s constituents with absorption line techniques has proven a powerful approach. Absorption line measurements, unlike studies of emission, are uniformly sensitive at all redshifts. Modern samples of absorption lines are large and spread over the whole sky are free from effects of cosmic variance, allowing us to delineate the global evolution of the baryonic properties of the Universe. In this review, we have explored the conclusions resulting from this simple, but powerful, counting of atoms in absorption line measurements. These include constraints on the global evolution of baryons, metals, and dust over 90% of cosmic time. Although some issues remain (see *Future Issues* box below), the cosmic evolution of these quantities is – in the broadest strokes – fairly secure (see *Summary Points* box below). Connecting this large scale view to the smaller scale is an exciting direction for future work.

SUMMARY POINTS

1. This review focused on the the global quantities of baryons, metals, and dust. It sought to relate the changes in these quantities to one another, as material cycled through the various phases of baryons with cosmic time.
2. The global densities of stars and neutral gas are well-constrained to $z \approx 5$. Observations are starting to provide new constraints on the molecular hydrogen density. Though there is significant work to be done to understand the systematics associated with deriving molecular densities from current CO measurements, we have now for the first time estimates of this quantity from high-redshift until $z=0$.
3. The shape of the molecular density with redshift is remarkably similar to that of the SFR density, pointing to a strong coupling between these quantities. The global density of condensed matter in stars and neutral and molecular material has increased with time, requiring the accretion of material from the ionized gas reservoir into these cold forms. The baryonic accretion rate density onto dark matter halos scaled by an efficiency factor shows a similar shape to the net condensed matter accretion rate. These results indicate that the low-redshift decline of the star-formation history is driven by the lack of molecular gas supply due to a drop in net accretion rate, which is itself driven by the decreased growth of dark matter halos. These observations are in remarkable agreement with the gas regulator model,

which describes a continual cycle of baryons flowing in and out of galaxies as a key moderator of galaxy evolution.

4. After correcting for dust depletion, the mean metallicity of the neutral gas in the Universe increases by $\approx 10\times$ over the redshift range $z \approx 5$ to ≈ 0 , whereas the global comoving metal density of neutral gas only increases by $\approx 4.5\times$ over that same period (due to the slowly decreasing gas density).
5. The metals in neutral gas dominates the metal content of the Universe at $z \gtrsim 2.5$, consistent with containing nearly all of the metals produced by stars to that point. The significant contributors to the metal budget diversify with time, with stars and hot gas becoming increasingly important hosts of metals. Although direct observational constraints are lacking at intermediate redshifts ($1 \lesssim z \lesssim 2$), modern censuses indicate that the metal content of the Universe is largely accounted for.
6. Analysis of dust depletion in neutral gas provides an estimate of dust properties up to $z \approx 5$. This analysis shows the dust content of neutral gas is a strong function of metallicity extending to below 1% of the solar metallicity. The global comoving dust density of neutral gas in the Universe increases by nearly 1 dex from $z \approx 5$ to $z \approx 1$ and is in agreement with estimates of dust mass in galaxies at $z < 2$.

FUTURE ISSUES

1. **Global evolution:** What approaches will be fruitful for improving the assessment of $\Omega_{\text{neutral gas}}$ at $z > 3.5$? What paths will allow us to better quantify the density of *ionized* gas, Ω_{H^+} ? How can we minimize the systematics in estimating $\Omega_{\text{molecular gas}}$? Are there better proxies for determining $\Omega_{\text{molecular gas}}$ (i.e., alternatives to CO)? How well can we simulate the colder phase of the gas in galaxies? How to observe directly the accretion implied by Figure 6? How to extend measurements of Ω_{dust} (§4.2) to earlier cosmic times, when the first grains are being formed? Which physical processes cause the observed evolution? Can we simulate them?
2. **Missing populations:** Is our current sample missing a population of absorbers (§3.2.3) that significantly biases the characterization of $\Omega_{\text{neutral gas}}$, Ω_{metals} , and Ω_{dust} ?
3. **Completing the metal census:** To what redshifts do metals in stars and the hot gas in groups and clusters contribute significantly to the metal census (§3.5.2)? How do we improve on measurements of the metal content at columns below those associated with neutral gas (§3.5.3)?
4. **Galaxy contributors:** What galaxy populations contribute most to the baryonic densities $\Omega_{\text{neutral gas}}$ and $\Omega_{\text{molecular gas}}$ as well as to the densities Ω_{metals} and Ω_{dust} ? How does the mix of contributions change with redshift?
5. **Spatial distribution of metals and dust about galaxies:** How are metals and dust distributed about galaxies and beyond (Figure 1)? How does this change with redshift? Is there pristine gas to be found? Can we reproduce the metal and dust distribution in simulations?

DISCLOSURE STATEMENT

The authors are not aware of any affiliations, memberships, funding, or financial holdings that might be perceived as affecting the objectivity of this review.

ACKNOWLEDGMENTS

CP thanks the Alexander von Humboldt Foundation for the granting of a Bessel Research Award held at MPA. JCH recognizes support from NSF grant AST-1517353. We are grateful to the following people for sharing data and for useful discussions: Shohei Aoyama, Annalisa de Cia, Valentina D’Odorico, Samuel Quiret, Nicolas Lehner, Ryan McKinnon, Dylan Nelson, Molly Peeples, and Jonghwan Rhee. We also wish to acknowledge insightful comments from George Becker, Nicolas Bouché, I-Da Chiang, Stefano Etti, Andrea Ferrara, Mike Fall, Masataka Fukugita, Michele Fumagalli, Reinhard Genzel, Ed Jenkins, Andrey Kravtsov, Varsha Kulkarni, Bruno Leibundgut, Piero Madau, Brice Ménard, Simon Morris, Max Pettini, Gergő Popping, Philipp Richter, Mike Shull, Linda Tacconi, Paolo Tozzi, Juan Vladilo, Rob Yates, Don York, Fabian Walter, Simon White, and Martin Zwaan.

LITERATURE CITED

- Abraham RG, van Dokkum PG. 2014. *PASP* 126:55
- Aller MC, Kulkarni VP, York DG, Welty DE, Vladilo G, Liger N. 2014. *ApJ* 785:36
- Aoyama S, Hou KC, Hirashita H, Nagamine K, Shimizu I. 2018. *MNRAS* 478:4905–4921
- Asplund M, Grevesse N, Sauval A, Scott P. 2009. *ARA&A* 47:481
- Augustin R, Quiret S, Milliard B, Péroux C, Vibert D, et al. 2019. *MNRAS* 489:2417–2438
- Bahcall J, Spitzer L. 1969. *ApJ* 156:L63
- Bauermeister A, Blitz L, Ma CP. 2010. *ApJ* 717:323–332
- Becker GD, Pettini M, Rafelski M, D’Odorico V, Boera E, et al. 2019. *ApJ* 883:163
- Becker GD, Sargent WLW, Rauch M, Calverley AP. 2011. *ApJ* 735:93
- Beeston RA, Wright AH, Maddox S, Gomez HL, Dunne L, et al. 2018. *MNRAS* 479:1077–1099
- Bekki K. 2015. *MNRAS* 449:1625–1649
- Bera A, Kanekar N, Chengalur JN, Bagla JS. 2019. *ApJL* 882:L7
- Berg TAM, Ellison SL, Sánchez-Ramírez R, López S, D’Odorico V, et al. 2019. *MNRAS* 488:4356–4369
- Berg TAM, Ellison SL, Sánchez-Ramírez R, Prochaska JX, Lopez S, et al. 2016. *MNRAS* 463:3021–3037
- Bird S, Garnett R, Ho S. 2017. *MNRAS* 466:2111–2122
- Bird S, Haehnelt M, Neeleman M, Genel S, Vogelsberger M, Hernquist L. 2015. *MNRAS* 447:1834–1846
- Bocquet S, Saro A, Dolag K, Mohr JJ. 2016. *MNRAS* 456:2361–2373
- Bolatto AD, Wolfire M, Leroy AK. 2013. *ARAA* 51:207–268
- Bolmer J, Ledoux C, Wiseman P, De Cia A, Selsing J, et al. 2019. *A&A* 623:A43
- Bouché N, Dekel A, Genzel R, Genel S, Cresci G, et al. 2010. *ApJ* 718:1001
- Bouché N, Finley H, Schroetter I, Murphy MT, Richter P, et al. 2016. *ApJ* 820:121
- Bouché N, Lehnert MD, Aguirre A, Péroux C, Bergeron J. 2007. *MNRAS* 378:525–540
- Bouché N, Lehnert MD, Péroux C. 2005. *MNRAS* 364:319–324
- Bouché N, Lehnert MD, Péroux C. 2006. *MNRAS* 367:L16–L19
- Bouché N, Murphy M, Péroux C, Contini T, Martin C, et al. 2012. *MNRAS* 419:2
- Carilli CL, Walter F. 2013. *ARA&A* 51:105–161

- Cashman FH, Kulkarni VP, Kisieliuss R, Ferland GJ, Bogdanovich P. 2017. *The Astrophysical Journal Supplement Series* 230:8
- Cen R, Ostriker JP. 1999. *ApJ* 514:1–6
- Chabrier G. 2003. *Publications of the Astronomical Society of the Pacific* 115:763–795
- Chang TC, Pen UL, Bandura K, Peterson JB. 2010. *Nature* 466:463–465
- Chen HW, Gauthier JR, Sharon K, Johnson SD, Nair P, Liang CJ. 2014. *MNRAS* 438:1435–1450
- Chen HW, Johnson SD, Zahedy FS, Rauch M, Mulchaey JS. 2017. *ApJL* 842:L19
- Chisari NE, Richardson MLA, Devriendt J, Dubois Y, Schneider A, et al. 2018. *MNRAS* 480:3962–3977
- Chiu I, Mohr JJ, McDonald M, Bocquet S, Desai S, et al. 2018. *MNRAS* 478:3072–3099
- Christensen L, Møller P, Fynbo JPU, Zafar T. 2014. *MNRAS* 445:225–238
- Churchill CW, Vander Vliet JR, Trujillo-Gomez S, Kacprzak GG, Klypin A. 2015. *ApJ* 802:10
- Cooke J, O’Meara JM. 2015. *ApJL* 812:L27
- Cooke RJ, Pettini M, Steidel CC. 2017. *MNRAS* 467:802–811
- Cooke RJ, Pettini M, Steidel CC. 2018. *ApJ* 855:102
- Crighton NHM, Murphy MT, Prochaska JX, Worseck G, Rafelski M, et al. 2015. *MNRAS* 452:217–234
- Cucchetti E, Pointecouteau E, Peille P, Clerc N, Rasia E, et al. 2018. *A&A* 620:A173
- Curran SJ. 2018. *Publications of the Astronomical Society of Australia* 35:36
- Davé R, Cen R, Ostriker JP, Bryan GL, Hernquist L, et al. 2001. *ApJ* 552:473–483
- Davé R, Finlator K, Oppenheimer BD. 2012. *MNRAS* 421:98–107
- Davé R, Rafieferantsoa MH, Thompson RJ. 2017. *MNRAS* 471:1671–1687
- Davies FB. 2019. *arXiv e-prints* :arXiv:1904.10459
- De Bernardis F, Cooray A. 2012. *ApJ* 760:14
- De Cia A. 2018. *A&A* 613:L2
- De Cia A, Ledoux C, Mattsson L, Petitjean P, Srianand R, et al. 2016. *A&A* 596:A97
- De Cia A, Ledoux C, Petitjean P, Savaglio S. 2018. *A&A* 611:A76
- de Graaff A, Cai YC, Heymans C, Peacock JA. 2019. *A&A* 624:A48
- De Vis P, Jones A, Viaene S, Casasola V, Clark CJR, et al. 2019. *A&A* 623:A5
- Decarli R, Walter F, Aravena M, Carilli C, Bouwens R, et al. 2016. *ApJ* 833:69
- Decarli R, Walter F, González-López J, Aravena M, Boogaard L, et al. 2019. *ApJ* 882:138
- Deharveng JM, Milliard B, Péroux C, Small T. 2019. *A&A* 623:A149
- Dekel A, Burkert A. 2013. *MNRAS* 438:1870
- Delhaize J, Meyer MJ, Staveley-Smith L, Boyle BJ. 2013. *MNRAS* 433:1398–1410
- Diemer B. 2018. *The Astrophysical Journal Supplement Series* 239:35
- Diemer B, Stevens ARH, Lagos CdP, Calette AR, Tacchella S, et al. 2019. *MNRAS* 487:1529–1550
- D’Odorico V, Cristiani S, Pomante E, Carswell RF, Viel M, et al. 2016. *MNRAS* 463:2690–2707
- D’Odorico V, Cupani G, Cristiani S, Maiolino R, Molaro P, et al. 2013. *MNRAS* 435:1198–1232
- Draine BT. 2011. *Physics of the Interstellar and Intergalactic Medium*
- Draine BT, Aniano G, Krause O, Groves B, Sandstrom K, et al. 2014. *ApJ* 780:172
- Draine BT, Li A. 2007. *ApJ* 657:810–837
- Driver SP, Andrews SK, da Cunha E, Davies LJ, Lagos C, et al. 2018. *MNRAS* 475:2891–2935
- Dunne L, Gomez HL, da Cunha E, Charlot S, Dye S, et al. 2011. *MNRAS* 417:1510–1533
- Ellison SL, Yan L, Hook IM, Pettini M, Wall JV, Shaver P. 2001. *A&A* 379:393–406
- Elson EC, Baker AJ, Blyth SL. 2019. *MNRAS* 486:4894–4903
- Emerick A, Bryan GL, Mac Low MM. 2019. *MNRAS* 482:1304–1329
- Faucher-Giguère CA. 2019. *arXiv e-prints* :arXiv:1903.08657
- Ferland GJ, Chatzikos M, Guzmán F, Lykins ML, van Hoof PAM, et al. 2017. *RMxAA* 53:385–438
- Ferrara A, Scannapieco E, Bergeron J. 2005. *ApJ* 634:L37–L40
- Foreman S, Coulton W, Villaescusa-Navarro F, Barreira A. 2019. *arXiv e-prints* :arXiv:1910.03597
- Forster-Schreiber N. 2020. *ARA&A* Submitted

- Frank S, Péroux C. 2010. *MNRAS* 406:2235–2248
- Fukugita M, Peebles PJE. 2004. *ApJ* 616:643–668
- Fumagalli M, O’Meara JM, Prochaska JX. 2011. *Science* 334:1245
- Fumagalli M, O’Meara JM, Prochaska JX. 2016. *MNRAS* 455:4100–4121
- Gaikwad P, Srianand R, Choudhury TR, Khaire V. 2017. *MNRAS* 467:3172–3187
- Gallazzi A, Bell EF, Zibetti S, Brinchmann J, Kelson DD. 2014. *ApJ* 788:72
- Gallazzi A, Brinchmann J, Charlot S, White SDM. 2008. *MNRAS* 383:1439–1458
- Geier SJ, Heintz KE, Fynbo JPU, Ledoux C, Christensen L, et al. 2019. *A&A* 625:L9
- Graziani L, Schneider R, Ginolfi M, Hunt LK, Maio U, et al. 2019. *arXiv e-prints* :arXiv:1909.07388
- Haardt F, Madau P. 2012. *ApJ* 746:125
- Hamanowicz A, Peroux C, Zwaan MA, Rahmani Hea. 2020. *MNRAS* Submitted
- Hamden ET, Hoadley K, Martin DC, Schiminovich D, Milliard B, et al. 2019. *FIREBall-2: advancing TRL while doing proof-of-concept astrophysics on a suborbital platform*. In *Proc. SPIE*, vol. 10982 of *Society of Photo-Optical Instrumentation Engineers (SPIE) Conference Series*
- Heintz KE, Fynbo JPU, Høg E, Møller P, Krogager JK, et al. 2018. *A&A* 615:L8
- Hoppmann L, Staveley-Smith L, Freudling W, Zwaan MA, Minchin RF, Calabretta MR. 2015. *MNRAS* 452:3726–3741
- Hou KC, Aoyama S, Hirashita H, Nagamine K, Shimizu I. 2019. *MNRAS* 485:1727–1744
- Hu W, Hoppmann L, Staveley-Smith L, Geréb K, Oosterloo T, et al. 2019. *MNRAS* 489:1619–1632
- Jenkins EB. 2009. *ApJ* 700:1299–1348
- Jenkins EB, Wallerstein G. 2017. *ApJ* 838:85
- Jones MG, Haynes MP, Giovanelli R, Moorman C. 2018. *MNRAS* 477:2–17
- Jorgenson RA, Wolfe AM, Prochaska JX, Lu L, Howk JC, et al. 2006. *ApJ* 646:730–741
- Junkkarinen VT, Cohen RD, Beaver EA, Burbidge EM, Lyons RW, Madejski G. 2004. *ApJ* 614:658–670
- Kanekar N, Prochaska JX, Smette A, Ellison SL, Ryan-Weber EV, et al. 2014. *MNRAS* 438:2131–2166
- Keating LC, Haehnelt MG, Cantalupo S, Puchwein E. 2015. *MNRAS* 454:681–697
- Kennicutt R. 1998. *ARAA* 36:189
- Kewley LJ, Ellison SL. 2008. *ApJ* 681:1183–1204
- Kewley LJ, Nicholls DC, Sutherland RS. 2019. *ARA&A* 57:511–570
- Khaire V, Srianand R. 2019. *MNRAS* 484:4174–4199
- Klitsch A, Péroux C, Zwaan MA, Smail I, Nelson D, et al. 2019a. *MNRAS* 490:1220–1230
- Klitsch A, Péroux C, Zwaan MA, Smail I, Oteo I, et al. 2018. *MNRAS* 475:492–507
- Klitsch A, Zwaan MA, Péroux C, Smail I, Oteo I, et al. 2019b. *MNRAS* 482:L65–L69
- Kovetz ED, Viero MP, Lidz A, Newburgh L, Rahman M, et al. 2017. *arXiv e-prints* :arXiv:1709.09066
- Kraljic K, Pichon C, Codis S, Laigle C, Davé R, et al. 2019. *arXiv e-prints* :arXiv:1910.08066
- Krogager JK, Fynbo JPU, Heintz KE, Geier S, Ledoux C, et al. 2016. *ApJ* 832:49
- Krogager JK, Fynbo JPU, Møller P, Noterdaeme P, Heintz KE, Pettini M. 2019. *MNRAS* 486:4377–4397
- Krumholz MR. 2013. *MNRAS* 436:2747–2762
- Kulkarni VP, Khare P, Péroux C, York DG, Lauroesch JT, Meiring JD. 2007. *ApJ* 661:88–94
- Lagos CDP, Baugh CM, Lacey CG, Benson AJ, Kim HS, Power C. 2011. *MNRAS* 418:1649–1667
- Lagos Cdp, Crain RA, Schaye J, Furlong M, Frenk CS, et al. 2015. *MNRAS* 452:3815–3837
- Leclercq F, Bacon R, Wisotzki L, Mitchell P, Garel T, et al. 2017. *A&A* 608:A8
- Lee CC, Webb JK, Carswell RF. 2019. *arXiv e-prints* :arXiv:1910.02913
- Lee KG, White M. 2016. *ApJ* 831:181
- Lehner N, O’Meara JM, Fox AJ, Howk JC, Prochaska JX, et al. 2014. *ApJ* 788:119
- Lehner N, Wotta CB, Howk JC, O’Meara JM, Oppenheimer BD, Cooksey KL. 2019. *arXiv e-prints* :arXiv:1902.10147

- Li Q, Narayanan D, Davé R. 2019. *MNRAS* 490:1425–1436
- Lilly SJ, Carollo CM, Pipino A, Renzini A, Peng Y. 2013. *ApJ* 772:119
- Lim SH, Mo HJ, Li R, Liu Y, Ma YZ, et al. 2018. *ApJ* 854:181
- Lopez S, Tejos N, Ledoux C, Barrientos LF, Sharon K, et al. 2018. *Nature* 554:493–496
- Madau P, Dickinson M. 2014. *ARA&A* 52:415
- Maddox N, Hewett PC, Péroux C, Nestor DB, Wisotzki L. 2012. *MNRAS* 424:2876–2895
- Maio U, Tescari E. 2015. *MNRAS* 453:3798–3820
- Maiolino R, Haehnelt M, Murphy MT, Quéloz D, Origlia L, et al. 2013. *arXiv e-prints* :arXiv:1310.3163
- Maiolino R, Mannucci F. 2019. *A&ARv* 27:3
- Mantz AB, Allen SW, Morris RG, Simionescu A, Urban O, et al. 2017. *MNRAS* 472:2877–2888
- Masui KW, Switzer ER, Banavar N, Bandura K, Blake C, et al. 2013. *ApJ* 763:L20
- McKinnon R, Vogelsberger M, Torrey P, Marinacci F, Kannan R. 2018. *MNRAS* 478:2851–2886
- McQuinn M. 2016. *Annual Review of Astronomy and Astrophysics* 54:313–362
- Ménard B, Fukugita M. 2012. *ApJ* 754:116
- Ménard B, Scranton R, Fukugita M, Richards G. 2010. *MNRAS* 405:1025–1039
- Merloni A, Predehl P, Becker W, Böhringer H, Boller T, et al. 2012. *arXiv e-prints*
- Millán-Irigoyen I, Mollá M, Ascasibar Y. 2019. *arXiv e-prints* :arXiv:1904.11215
- Momose R, Ouchi M, Nakajima K, Ono Y, Shibuya T, et al. 2016. *MNRAS* 457:2318–2330
- Murphy MT, Bernet ML. 2016. *MNRAS* 455:1043–1059
- Murphy MT, Kacprzak GG, Savorgnan GAD, Carswell RF. 2019. *MNRAS* 482:3458–3479
- Neeleman M, Prochaska JX, Zwaan MA, Kanekar N, Christensen L, et al. 2016. *ApJ* 820:L39
- Nelson D, Springel V, Pillepich A, Rodriguez-Gomez V, Torrey P, et al. 2019. *Computational Astrophysics and Cosmology* 6:2
- Noterdaeme P, Laursen P, Petitjean P, Vergani S, Maureira M, et al. 2012. *A&A* 540:63
- Noterdaeme P, Ledoux C, Zou S, Petitjean P, Srianand R, et al. 2018. *A&A* 612:A58
- Noterdaeme P, Petitjean P, Ledoux C, Srianand R. 2009. *A&A* 505:1087
- Oliveira CM, Sembach KR, Tumlinson J, O’Meara J, Thom C. 2014. *ApJ* 783:22
- O’Meara JM, Lehner N, Howk JC, Prochaska JX, Fox AJ, et al. 2017. *AJ* 154:114
- Padmanabhan H, Loeb A. 2020. *MNRAS* 496:1124–1131
- Pagel BEJ. 1999. *arXiv e-prints* :astro-ph/9911204
- Palanque-Delabrouille N, Magneville C, Yèche C, Pâris I, Petitjean P, et al. 2016. *A&A* 587:A41
- Pallottini A, Ferrara A, Decataldo D, Gallerani S, Vallini L, et al. 2019. *MNRAS* 487:1689–1708
- Papastergis E, Cattaneo A, Huang S, Giovanelli R, Haynes M. 2012. *ApJ* 759:138
- Parks D, Prochaska JX, Dong S, Cai Z. 2018. *MNRAS* 476:1151–1168
- Peebles M, Tumlinson J, Fox A, Aloisi A, Fleming S, et al. 2017. The Hubble Spectroscopic Legacy Archive. Tech. rep.
- Peebles MS, Corlies L, Tumlinson J, O’Shea BW, Lehner N, et al. 2019. *ApJ* 873:129
- Peebles MS, Werk JK, Tumlinson J, Oppenheimer BD, Prochaska JX, et al. 2014. *ApJ* 786:54
- Péroux C, Dessauges-Zavadsky M, D’Odorico S, Kim TS, McMahon RG. 2007. *MNRAS* 382:177–193
- Péroux C, McMahon RG, Storie-Lombardi LJ, Irwin MJ. 2003. *MNRAS* 346:1103–1115
- Péroux C, Rahmani H, Arrigoni Battaia F, Augustin R. 2018. *MNRAS* 479:L50–L54
- Péroux C, Rahmani H, Quiret S, Pettini M, Kulkarni V, et al. 2017. *MNRAS* 464:2053–2065
- Péroux C, Zwaan MA, Klitsch A, Augustin R, Hamałowicz A, et al. 2019. *MNRAS* 485:1595–1613
- Pettini M. 1999. *Element Abundances at High Redshifts*. In *Chemical Evolution from Zero to High Redshift*, eds. JR Walsh, MR Rosa
- Pichon C, Vergely JL, Rollinde E, Colombi S, Petitjean P. 2001. *MNRAS* 326:597–620
- Planck Collaboration, Ade PAR, Aghanim N, Arnaud M, Ashdown M, et al. 2016. *A&A* 594:A13
- Popping G, Pillepich A, Somerville RS, Decarli R, Walter F, et al. 2019. *ApJ* 882:137
- Popping G, Somerville RS, Galametz M. 2017. *MNRAS* 471:3152–3185

- Poudel S, Kulkarni VP, Morrison S, Péroux C, Som D, et al. 2018. *MNRAS* 473:3559–3572
- Pozzi F, Calura F, Zamorani G, Delvecchio I, Gruppioni C, Santini P. 2019. *MNRAS* :2378
- Prochaska J, Wolfe A. 2009. *ApJ* 696:1543
- Prochaska JX, Zheng Y. 2019. *MNRAS* 485:648–665
- Pullen AR, Serra P, Chang TC, Doré O, Ho S. 2018. *MNRAS* 478:1911–1924
- Putman ME. 2017. *An Introduction to Gas Accretion onto Galaxies*. In *Gas Accretion onto Galaxies*, eds. A Fox, R Davé, vol. 430 of *Astrophysics and Space Science Library*
- Quiet S, Péroux C, Zafar T, Kulkarni VP, Jenkins EB, et al. 2016. *MNRAS* 458:4074–4121
- Rafelski M, Neeleman M, Fumagalli M, Wolfe AM, Prochaska JX. 2014. *ApJ* 782:L29
- Rahmani H, Péroux C, Augustin R, Husemann B, Kacprzak GG, et al. 2018. *MNRAS* 474:254–270
- Rahmani H, Péroux C, Turnshek DA, Rao SM, Quiet S, et al. 2016. *MNRAS* 463:980–1007
- Rahmati A, Pawlik AH, Raičević M, Schaye J. 2013. *MNRAS* 430:2427–2445
- Rahmati A, Schaye J. 2014. *MNRAS* 438:529–547
- Rao SM, Turnshek DA, Sardane GM, Monier EM. 2017. *MNRAS* 471:3428–3442
- Rémy-Ruyer A, Madden SC, Galliano F, Galametz M, Takeuchi TT, et al. 2014. *A&A* 563:A31
- Rhee J, Lah P, Briggs FH, Chengalur JN, Colless M, et al. 2018. *MNRAS* 473:1879–1894
- Rhee J, Lah P, Chengalur JN, Briggs FH, Colless M. 2016. *MNRAS* 460:2675–2686
- Rhee J, Zwaan MA, Briggs FH, Chengalur JN, Lah P, et al. 2013. *MNRAS* 435:2693–2706
- Richings AJ, Schaye J, Oppenheimer BD. 2014. *MNRAS* 442:2780–2796
- Riechers DA, Pavesi R, Sharon CE, Hodge JA, Decarli R, et al. 2019. *ApJ* 872:7
- Rubin KHR, Diamond-Stanic AM, Coil AL, Crighton NHM, Moustakas J. 2018. *ApJ* 853:95
- Saintonge A, Catinella B, Tacconi LJ, Kauffmann G, Genzel R, et al. 2017. *ApJS* 233:22
- Saintonge A, Kauffmann G, Wang J, Kramer C, Tacconi LJ, et al. 2011. *MNRAS* 415:61–76
- Sánchez-Ramírez R, Ellison SL, Prochaska JX, Berg TAM, López S, et al. 2016. *MNRAS* 456:4488–4505
- Savage BD, Sembach KR. 1991. *ApJ* 379:245
- Schaye J, Carswell RF, Kim TS. 2007. *MNRAS* 379:1169–1194
- Semboloni E, Hoekstra H, Schaye J, van Daalen MP, McCarthy IG. 2011. *MNRAS* 417:2020–2035
- Shull JM, Danforth CW, Tilton EM. 2014. *ApJ* 796:49
- Shull JM, Smith BD, Danforth CW. 2012. *ApJ* 759:23
- Steidel C, Bogosavlejevic M, Shapley A, Kollmeier J, Reddy N, et al. 2011. *ApJ* 736:160
- Stern J, Hennawi JF, Prochaska JX, Werk JK. 2016. *ApJ* 830:87
- Tacconi LJ, Genzel R, Saintonge A, Combes F, García-Burillo S, et al. 2018. *ApJ* 853:179
- Tacconi LJ, Genzel R, Sternberg A. 2020. *ARA&A* Submitted
- Tanimura H, Hinshaw G, McCarthy IG, Van Waerbeke L, Aghanim N, et al. 2019. *MNRAS* 483:223–234
- Teyssier R, Commerçon B. 2019. *Frontiers in Astronomy and Space Sciences* 6:51
- Thacker C, Cooray A, Smidt J, De Bernardis F, Mitchell-Wynne K, et al. 2013. *ApJ* 768:58
- Tumlinson J, Peebles MS, Werk JK. 2017. *ARA&A* 55:389–432
- Tytler D. 1982. *Nature* 298:427–432
- Vijayan AP, Clay SJ, Thomas PA, Yates RM, Wilkins SM, Henriques BM. 2019. *MNRAS* 489:4072–4089
- Vílchez JM, Relaño M, Kennicutt R, De Looze I, Mollá M, Galametz M. 2019. *MNRAS* 483:4968–4983
- Vladilo G. 2004. *A&A* 421:479–490
- Vladilo G, Centurión M, Bonifacio P, Hawk JC. 2001. *ApJ* 557:1007–1020
- Vladilo G, Péroux C. 2005. *A&A* 444:461–479
- Walter F, Decarli R, Sargent M, Carilli C, Dickinson M, et al. 2014. *ApJ* 782:79
- Werk J, Prochaska J, Thom C, Tumlinson J, Tripp T, et al. 2013. *ApJS* 204:17
- Werk JK, Prochaska JX, Tumlinson J, Peebles MS, Tripp TM, et al. 2014. *ApJ* 792:8
- Westmeier T. 2018. *MNRAS* 474:289–299

- Wijers NA, Schaye J, Oppenheimer BD, Crain RA, Nicastro F. 2019. *MNRAS* 488:2947–2969
- Wisotzki L, Bacon R, Brinchmann J, Cantalupo S, Richter P, et al. 2018. *Nature* 562:229–232
- Wolfe AM, Gawiser E, Prochaska JX. 2005. *ARA&A* 43:861–918
- Wolfe AM, Turnshek DA, Smith HE, Cohen RD. 1986. *The Astrophysical Journal Supplement Series* 61:249
- Wotta CB, Lehner N, Howk JC, O’Meara JM, Oppenheimer BD, Cooksey KL. 2019. *ApJ* 872:81
- Wotta CB, Lehner N, Howk JC, O’Meara JM, Prochaska JX. 2016. *ApJ* 831:95
- Wright AH, Driver SP, Robotham ASG. 2018. *MNRAS* 480:3491–3502
- Yates RM, Thomas PA, Henriques BMB. 2017. *MNRAS* 464:3169–3193
- Zafar T, Péroux C, Popping A, Milliard B, Deharveng J, Frank S. 2013. *A&A* 556:141